## Anonymous Referee #1

### General comments

I would like to thank the authors for addressing the comments given on the first round of revisions. There are a few more comments that I would like the authors to address before publication. Below are the original comments, authors responses start with * and new comments with _.

First of all, we would like to thank the reviewer for the positive evaluation and providing important comments. We hope that all your concerns will be cleared after reading our responses and modifications made to the manuscript. Please find below our answers (in green) and modifications (deleted in red and added in blue) to your comments/suggestions/questions.

### Specific comments

Mahmud et al 2018 showed that different sea ice types have different incidence angle dependent slopes. Have you considered using a sea ice type dependent slope factor? Moreover, how does the work by Mahmud et al 2018 fit in with the incidence angle dependencies presented here?
*Typically, the slope for open water is higher than that for sea ice, thus the correction works in a way reducing the difference in sigma naught for open water as well. As the review pointed, different sea ice types have different incidence angle dependent slopes; however again, ice type-specific correction prior to ice type classification is controversial. Although estimating ice type dependent slope is not a part of this manuscript, we provide the values derived from the training/validation dataset for the review purpose only.
_Studying the figures provided in the review, the HV sigma naught values for the different ice types and open water used in the training/validation data, it is striking that there is hardly any variation across incidence angle, but also that there is limited difference in backscatter values between the different types of surface. The values in the HV- data presented appear to be very low, especially considering that there is a difference in the backscatter values, e.g. for the open water, presented in Figure 7 and 8. As a side note would a scalebar in dB for Figure 7 and 8 be beneficial. Moreover, the values are close to the nominal noise floor provided with the meta data in the Sentinel-1 images. Is the lack of trend an effect of the thermal noise correction applied to the images?
_Work by e.g. Isleifson et al 2010 found slopes for new ice and all 4 channels given a range of incidence angles and sufficient SNR. Work by Gill et al 2015 also found slopes of -0.25 for the HV-channel and Scharien et al, 2014 also found slopes for the HV-channel. How does this work relate to those studies?

We had made a mistake in estimating the incidence angle dependence in our previous results. After subtracting the thermal noise power, we had added the mean noise power back to the denoised image in order to prevent the denoised sigma naught in linear scale from falling down into negative values. As adding offset in linear scale is equivalent to scaling in log scale (decibel), the incidence angle dependence estimated in log scale had been corrupted. After revising this problem, we got new results summarized in the figure below.

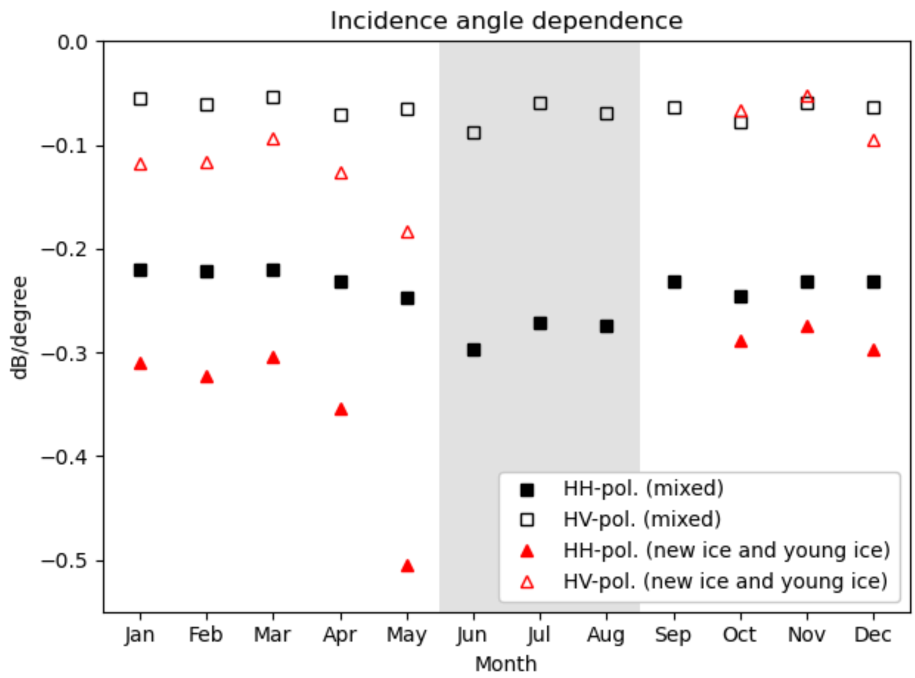


The averaged incidence angle dependences of mixed ice types (squares) in mid-winter season (Jan-Mar) are -0.21 and -0.06 for HH and HV polarizations, respectively. These values are lower than those in our previous results, which were -0.200 and -0.025 for HH and HV polarizations, respectively. The values of new and young ice (triangles) are much lower especially when the season is close to summer. The large slope of -0.18 for HV polarization in May is comparable to the findings in Gill et al. (2015), which is -0.25 estimated from smooth first-year ice in May. Based on the reprocessed results, we changed Figure 4 and added explanations in revised manuscript.

**[page 4, line 31-32] and [page 5, line 1-3]**

of the satellite orbit and image acquisition geometry. By following the methods developed in Park et al. (2018, 2019), each of the Sentinel-1 images was denoised before further processes are applied. As the noise power subtraction yields negative intensity values where the backscattering power is close to the noise floor, especially in HV polarization, we added mean of the noise power back to the denoised result so that those pixels do not turn into NaN (not a number) by the sigma naught conversion of linear scale to log scale (decibel).

**[page 5, lines 15-31]**

~~Figure 4 shows two dimensional histograms of incidence angle versus sigma nought for sea ice pixels in HH and HV polarization channels from Sentinel-1 data collected over sea ice and open water in the study area in winter 2018.~~ Figure 4 shows incidence angle dependence in the SAR backscattering intensity for mixed sea ice types. From the Sentinel-1 dataset described in Section 2.1, sea ice pixels were extracted by using daily global sea ice edge products available from the EUMETSAT Ocean and Sea Ice Satellite Application Facilities (OSI SAF). For mid-winter season (Jan-Mar displayed by blue background), ~~For HH polarization,~~ the estimated mean slope in HH polarization was ~~-0.200~~-0.21 dB/degree, which is slightly different from the estimation of the first-year ice (-0.24 dB/degree) in Mäkynen and Karvonen (2017) and in between the estimations for first-year ice (-0.22 dB/degree) and multi-year ice (-0.16 dB/degree) in Mahmud et al. (2018). For HV polarization, the estimated slope was only ~~-0.025~~-0.06 dB/degree, which is much lower than ~~the estimation~~-0.16 dB/degree for deformed first-year ice in Mäkynen and Karvonen (2017), however, it is in line with the estimations ~~from RADARSAT-2 (Leigh et al., 2014; Liu et al., 2015).~~in Liu et al., 2015. Work by Leigh et al. (2014) stated that the HV polarization backscatter signatures are largely unaffected by incidence angle variation in their RADARSAT-2 dataset. For summer season (Jun-Aug displayed by red background), the mean slopes increased to -0.28 and -0.08 dB/degree in HH and HV polarization, respectively. Scharien et al. (2014) reported significant slopes for ice adjacent to melt ponds in June, and Gill et al. (2015) also found slopes of -0.33 and -0.25 for smooth first-year ice in May in HH and HV polarization, respectively. The smaller slopes in our estimation are likely due to the mixed ice types and structures; the SAR backscattering of deformed ice has lower incidence angle dependency as shown in Mäkynen and Karvonen (2017).

**[Figure 4] – replaced**

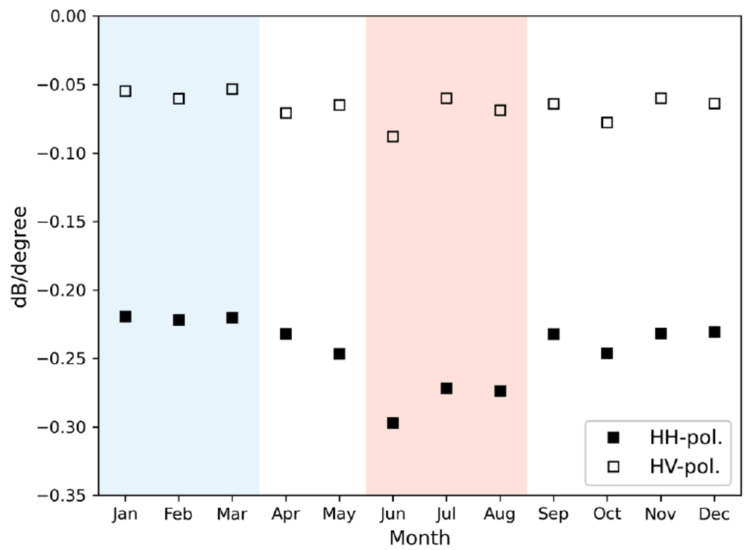


**Figure 4: Incidence angle dependences of sigma naught in HH (closed squares) and HV (open squares) polarization channels. Pixels covering various types of sea ice were merged so that the averaged property can be estimated. The blue and red zones indicate winter and summer seasons, respectively.**

How do you define "good match" (P7 R3)? Temporal overlap? Spatial overlap? How was this manual selection of images performed? How were the open water vs sea ice charts, that are used as initial input into the classifier, derived?

*Both temporal and spatial overlaps are important. Since the SAR image itself is potentially one of the sources for ice charting at the ice services, some images spatially match well with the shape of the polygons in ice chart. Temporal window length of 3 days from the publication date of ice chart was used for squeezing the number of images to make decisions of use/discard for training.

_What is a good match? Please state this clearly in the manuscript. The sentence now simply states that spatially and temporally good matches were used. How large is the spatial overlap? What is meant with squeezing the number of images?

As no scene identifiers or time window information of the satellite image products used for ice charting are annotated in the ice chart, is it crucial to identify SAR image – ice chart pairs sharing the same time instance or ice conditions. The good match in this study is the visual fitness of the ice-water boundaries. "Temporal window length of 3 days from the publication date of ice chart" is the time window of source information publication date annotated in the XML data comes with ice chart. As the time window does not cover the entire 7 days in week, only the images acquired from 3 days prior to the date of ice chart publication need to be examined, and this is what we meant with "squeezing the number of images". We added explanations in revised manuscript.

**[page 8, lines 9-26]**

To train an ice type classifier, a set of collocated SAR images and ice charts is required. After the preprocessing of the ice chart including reprojection into the SAR image geometry, only the samples with spatially and temporally good matches should be fed to the training phase. The goodness of matching should be examined as the weekly ice chart is produced by merging information from many image sources acquired in different time instances, hence the ice locations and conditions are unlikely match to those in every SAR image. As no explicit scene identifier or time information of the images used in ice charting is provided with the ice chart itself, the basic strategy in image selection is to find a pair of SAR image and ice chart which match well visually. Such an i~~I~~mage selection is trivial, but not easy to automate. Since the weekly ice chart is made partly based on the SAR images acquired in the past three days from the date of publication, the ice edges in some images match well with those in the ice chart.

In order to automate image selection, the ice edges in SAR images need to be identified first. Since even an ice/water classifier has not been well developed yet for Sentinel-1, the image selection procedure has to be done manually in the beginning. However, once a classifier is generated with high accuracy, it can be used to automate the procedure, then the whole process in the proposed scheme will be fully automated. This is why the proposed algorithm is named "semi-" automated for now. Nevertheless, the manual selection to guarantee a "good match" is done by visual inspection of ice-water boundaries overlaid on SAR images. The ice-water boundary can be extracted easily from the reprojected ice chart ~~by selecting the pixel borders of open water class~~. Then the SAR backscattering image contrasts across the ice-water boundaries are examined both in HH- and HV-polarization because the image contrast between ice-water is larger in HV ~~and~~ while smooth level ice is ~~better recognizable~~more easily identified in HH.

Figure 8. In Figure 3 and 7 the ice chart from 3 days later is used yet in Figure 8 the image from the same day is used. Please be consistent in which time interval is used for these weekly ice charts.
*Since the reference ice chart is published weekly, the same NIC ice chart both in Figure 7 and 8 is supposed to be valid for both dates of Figure 7 and 8, but it is not as shown. The common time interval of 3 days in Figure 3 and 7 is just a coincidence. It can be one day or two days depending on the date of SAR image that used as source materials for ice charting at ice services. If the satellite images acquired two days prior to the publication of weekly ice chart, then the overall distribution of ice would represent the status of that time. Note that among the 57 images used for training, 42 and 35 percent of the images were acquired 2 and 3 days prior to the publication date of the corresponding weekly ice chart, respectively.
_For the validation data in 2018 and 2019 how many of those images were acquired at 2 and 3 days prior to the ice chart used to validate them?

The distribution of the number of images in the extended dataset of the revised manuscript is added to the revised manuscript.

**[page 9, lines 3-7]**

phase. Among ~~958~~ 4485 images in total, we selected ~~57~~ 840 images (419 for winter season and 421 for summer season) of which ice edges match well with the collocated ice chart. From the selected images, ~~6.4~~120 million samples covering open water and sea ice were divided into training and test dataset. The DS2 was used to evaluate the performance of the trained classifier using temporally independent dataset of 513 images (281 for winter season and 232 for summer season). The distribution of the image acquisition dates prior to the publication of the reference ice chart is shown in Table 2.

**[Table 2]**

**Table 2: Distribution of the image acquisition dates prior to the publication of the reference ice chart**

| | Training and test dataset (DS1) | | | | Validation dataset (DS2) | | | |
|---|---|---|---|---|---|---|---|---|
| Days prior to the date of ice chart publication | 3 | 2 | 1 | 0 | 3 | 2 | 1 | 0 |
| Winter | 124 | 168 | 77 | 50 | 78 | 75 | 67 | 61 |
| Summer | 119 | 125 | 112 | 65 | 87 | 67 | 48 | 30 |

_The new ice areas likely change at short time scales. What is the impact of having 42% (2-days) and 35% (3-days) time separation between the image acquisition and the sea ice chart? Is there a consistent time difference between the 2018 and 2019 data with respect to the Sentinel-1 images and the sea ice charts? Comparing the accuracy of the sea ice classifications with the temporal difference might provide some answers here.

As in the table above, the is no consistent time difference between DS1 and DS2.

## Technical comments

In many places references to the appropriate work is missing, e.g. P1, R27, P4 R15-16 and P6 R9-10. Please carefully revise the manuscript to include references to earlier work.
*Corrected.
_The P6 R9-10 still has no reference to previous work.
Corrected.

P6 R10-12 you argue that when training dataset are prepared manually the sample size is usually less then 20 images. Please provide several references to support this statement.

_In Liu et al 2015 only one image is used for the training data please revise the manuscript accordingly (P6 R29). Another image is used for the validation of their study but only one for the training data.
Corrected.

_The reference Leigh et al 2014 does not provide slopes for either the HH- or the HV-channel in their study. Please revise the manuscript accordingly.
Corrected.

In Figure 9 the sea ice type FYI thin is include in the sea ice classification results. Please clarify what thin FYI means. Why is this class not used throughout?
*The label was wrong. It was just FYI without "thin". As the bottom panels (SAR results) are irrelevant in the context of the corresponding description, they were removed in the revised manuscript.
_In Figure 9 the label thin FYI is still present.
This is because Figure 9 displays the original SoDs in the NIC ice chart, not the simplified SoDs of the proposed method. We added an explanation to the caption of Figure (now Figure 11) in the revised manuscript.

**[Figure 9]**

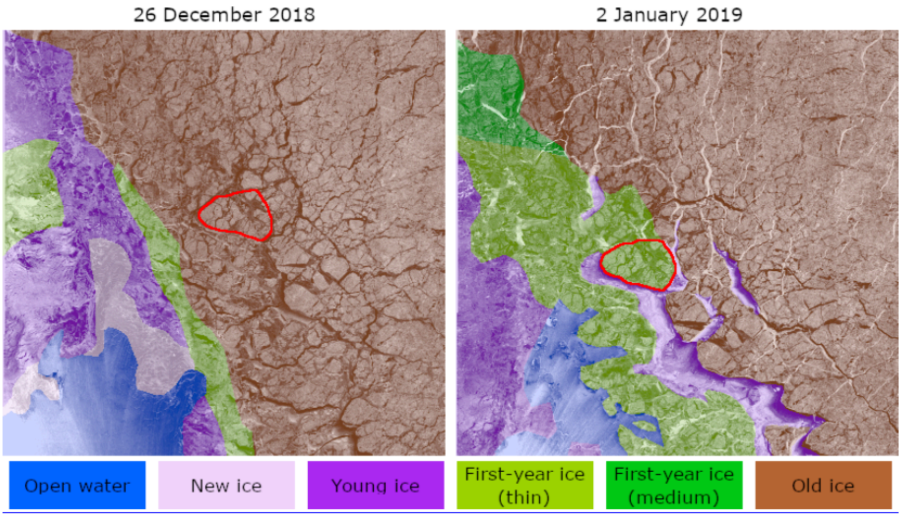


Figure 11: An example of the inconsistency of the ice charts. Note that the SoD labels and colors are of original NIC ice chart, while those in Figure 7 and 8 are of simplified version as described in Section 2.2.1.The SoDs from the NIC ice charts on different dates (26 December 2018 and 2 January 2019) are superimposed on the Sentinel-1 backscattering image of the corresponding dates. The same ice floe (red outline) is classified differently in each ice chart (old ice on the left panel and first-year ice on the right panel) despite of the similarity in the SAR backscattering images.

_Throughout the manuscript first year ice is not consistently named: e.g. Figure 3 FYI (top left) FY ice (bottom left), Figure 7 and 8 First-year ice. Page 3, Row 9. First year. Moreover, FYI is not defined within the manuscript.
Corrected.

_P1 R11. Number -> amount
Corrected.

_P1. R20 What is operational manner?
Corrected.

_P2. R1-3. Reference to "HH and HV widely used for ice edge detection etc" is missing.
Corrected.

_P2. R29-30. Please specify type of bias.
Corrected.

_P4. R.23 "...noise, some which originate..."
Corrected.

_P8 R13. Clarify easily or remove it. "...borders of the open water ..."
Corrected.

_P8 R13-15. Unclear sentence please revise.
Corrected.

_P10 R18. For FC1 and FC2 there is an improvement, however for FC3 there is a -0.05 reduction in the Kappa values. Please revise the sentence to account for this.
Corrected.

_P11 R20. "different marginal sides". What does this mean?
Corrected. "different edges of the range swath"

_P11 R21. Which figure is this image boundary visible in?
Corrected.

_P11 R22. What does extreme marine conditions mean? Please clarify.
Corrected.

_P11 R23-25. Are high wind conditions not accounted for/included in your training data?
An explanation regarding this misclassification was added to the revised manuscript.

**[page 12, lines 24-29]**

8, there is a misclassified ~~FYI~~ first-year ice patch (yellow) in the open water area. According to the high resolution sea surface winds data from SAR on the Sentinel-1 satellites (https://data.nodc.noaa.gov/cgi-bin/iso?id=gov.noaa.nodc:SAR-WINDS-S1)~~NOAA SAR wind image service, ANSWRS 2.0~~, the wind speed ranged from 17 to 21 m/s at the time of image acquisition heavily roughing the water surface. Although we have included images with both high and low wind conditions in our training data, the image textures of wind roughened water surface and ice were confused in some cases, and the same happened in the image textures of calm water surface and smooth level ice.

## Anonymous Referee #2

The manuscript has been improved as compared to the previous version. However, there are still points to which I would like to hear from the authors:

First of all, we would like to thank the reviewer for the positive evaluation and providing important comments. We hope that all your concerns will be cleared after reading our responses and modifications made to the manuscript. Please find below our answers (in green) and modifications (deleted in red and added in blue) to your comments/suggestions/questions.

1. The authors do not give guidance as to the accuracy of the NIC chart ice type information. It is difficult to assess the quality of the classifier output when it is trained with, and evaluated against, only NIC charts. The accuracy could be investigated by comparing NIC charts with Canadian ice service charts for regions/dates on which both are available. Alternatively, the output from the classifier (ice type) should be compared against another data source (eg. OSI-403-c).

   By adopting the reviewer's suggestion, we compared the output of our three-class classifiers against the OSI SAF sea ice type product, OSI-403-c, and the corresponding results and discussions were included in the revised manuscript.

**[page 11, lines 32-35] and [page 12, lines 1-14]**

Unfortunately, we could not find an official report regarding the accuracy of the NIC ice chart information. It might be not enough to assess the quality of the classifier output when it is trained with, and evaluated against, only NIC ice charts. The accuracy could be indirectly investigated by comparing the output from our classifier against another data source, such as OSI SAF sea ice type product (OSI-403-c). The ice classes of OSI-403-c are assigned from atmospherically corrected brightness temperatures of passive microwave radiometers (SSMIS and AMSR2) and backscatter values of radar scatterometer (ASCAT), using a Bayesian approach (Aaboe et al., 2018). Table 10 shows the confusion matrices for our three-class classifiers when their prediction results are compared with the OSI-403-c product as reference. Comparing with the results in Table 9, the accuracies for open water decreased from by 6%; however, this is mainly because the ice concentration threshold for ice-water discrimination in OSI-403-c is 35% which is higher than 20% that we set in our preprocessing of NIC ice chart (Section 2.2.1), thus areas with low ice concentration in marginal ice zone are most likely annotated as open water in OSI-403-c. For first-year ice, large portions (72%) are misclassified as old ice. This might be partly explained from the Figure 12, which shows the ice classes in NIC ice chart and OSI-403-c for the same publication date. A large extent of old ice in NIC ice chart is annotated as multi-year ice in OSI-403-c. As our classifiers were trained with NIC ice chart, it is natural to result in more old ice for the area where the ice type is classified as first-year ice in OSI-403-c. For old ice, the accuracy was the highest, 98%. Finding the reason for the clear discrepancy of the extent of first-year ice between the NIC ice chart and OSI-403-c is beyond the scope of this study, however, it should be noted that an elaborate future work for cross calibrating ice types in different ice charts are necessary.

**[Table 10]**

**Table 10: Confusion matrix of the three-class RF classifier which was trained with DS1 winter dataset and applied to the DS2 winter dataset with reference to OSI SAF sea ice type product (OSI-403-c)**

| | | Predicted (classifier was trained with NIC ice chart) | | | | | | | | |
|---|---|---|---|---|---|---|---|---|---|---|
| | | Open water | | | Mixed first-year ice | | | Old ice | | |
| | Case | FC1 | FC2 | FC3 | FC1 | FC2 | FC3 | FC1 | FC2 | FC3 |
| Reference (OSI SAF) | Open water | **85.9** | **86.1** | **86.2** | 12.6 | 12.4 | 12.1 | 15.7 | 15.3 | 16.2 |
| | First-year ice | 1.9 | 1.6 | 2.0 | **26.0** | **26.8** | **26.9** | 72.1 | 71.6 | 71.2 |
| | Multi-year ice | 0.1 | 0.1 | 0.1 | 1.5 | 1.4 | 1.4 | **98.4** | **98.5** | **98.5** |

**[Figure 11]**

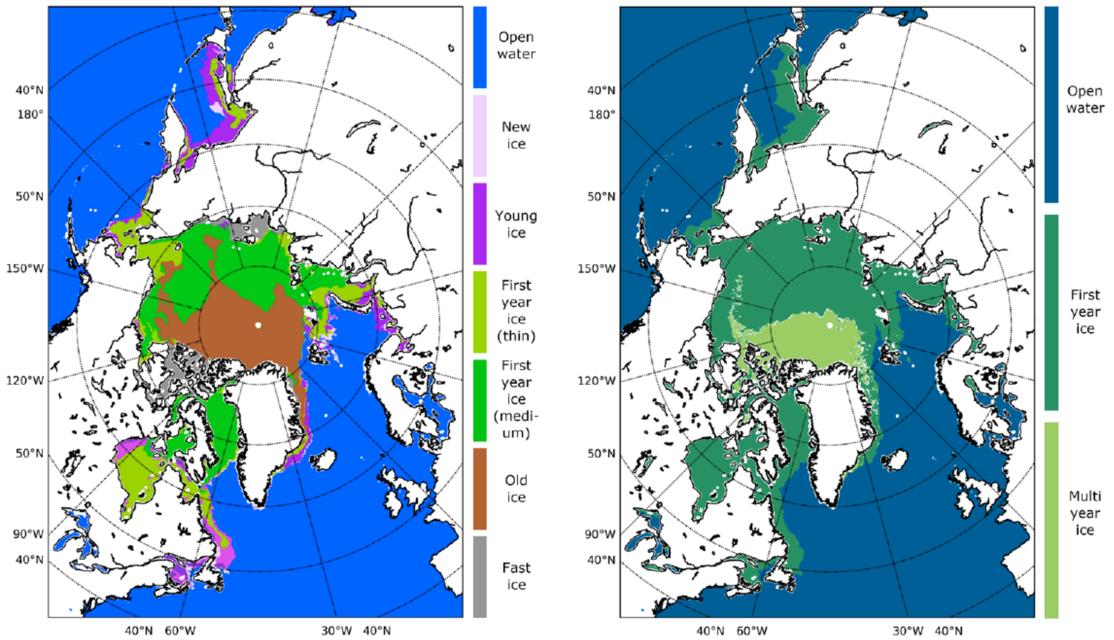


**Figure 12: The ice types in NIC ice chart (left) and OSI SAF sea ice type product (right) for the same date (8 Jan. 2019). Note that the SoD labels and colors follows those defined in each ice chart format.**

2. The contribution of the study still needs to be clarified. I don't feel that the main technological innovations claimed in the conclusions have been demonstrated. There is no clear demonstration that the time in running the semi-automated method is much less than the manual approach (in particular given that there is a manual step in the method, and given the tools available to pull samples from images that could be used in a study that is manually generating samples), nor is it clear to me how the evaluation of the classifier is more objective (more objective as compared to what? another method? or independent data? see above comment).

Additional experimental results were added to the manuscript and the conclusions were revised.

**[page 12, line 30-32] and [page 13, line 1-18]**

**4 Conclusion**

A new semi-automated SAR-based sea ice type classification scheme was proposed in this study. For the first time several ice types ~~can be~~were successfully identified on Sentinel-1 SAR imagery in winter season, while only an ice-water discrimination was feasible in summer season. The main technological innovation is two-fold: i) minimized manual work in the preparation of training and validation reference data and ii) more objective evaluation of the SAR-based sea ice type classifier compared to the previous studies conducted with small number of images and customized ice type references from informal sources. A conventional approach for selecting training/testing data by anonymous human ice expert is undesirable not only because it is laborious, but also due to subjectivity and lack of standardization in the assessment of the automated classifier. Therefore, the performance from different literature sources cannot be intercompared directly.

Test results from the datasets of ~~two winter seasons~~winter season acquired over the Fram Strait and the Barents Sea area showed overall accuracies of ~~85% and 58%~~87% and 60% and the Cohen's kappa coefficients ~~κ~~ of ~~0.80 and 0.67~~0.75 and 0.67 for the three-class and five-class ice type classifiers, respectively. These are slightly lower than the numbers in the previous studies, and the errors are attributed not only to the automated algorithm but also to the inconsistency of the ice charts and the high level of their generalization. Test results from the datasets of summer seasons showed overall accuracy of 67% and the Cohen's kappa coefficient of 0.78 for the three-class classifiers. Considering the misclassifications in different ice types were among themselves, the three-class classifiers performed well at least as an ice-water discriminator with accuracy of 98%.

Based on the results, we envisage that three-class ice type classification from SAR imagery would be useful for making a global sea ice type product like ~~EUMETSAT OSI-403-C~~OSI SAF OSI-403-c with higher spatial resolution. The proposed approach importantly showed that a daily ice type mapping from the Sentinel-1 data is feasible and can help capture details of short-term changes in the stage of sea ice development. Based on the achieved results, we believe that the proposed approach may be efficiently used for operational ice charting services for supporting navigation in the Arctic.

3. This study does demonstrate several important problems that need to be resolved when using ice type from operational charts to train a classifier. For example, the labels from NIC have accuracy issues (or inconsistency issues as stated in the conclusions), there seem to be possible issues with the incidence angle correction etc. How do the authors propose moving forward? For example, if the authors are really proposing a higher resolution three-class classification, how are they first planning to overcome the problems observed in the present study? A thoughtful discussion of these issues would be a nice contribution.

   The discussions and conclusion were revised.

**[page 12, lines 15-29]**

~~Unfortunately, t~~The proposed algorithm has several limitations. First of all, the variations in radar backscattering and its corresponding image textures due to seasonal changes were not properly captured. Although day-of-the-year was tested as a seasonality variable in the FC3 feature configuration, the result did not show any improvement. This is because ~~day-of-the-year might not correspond to the same temperature, fluxes, and weather regimes~~ SAR image features, which partially reflect temperature fluxes and weather regimes, might not correspond to day-of-the-year. Second, the proposed method struggles when the same type of sea ice is located on different ~~marginal sides~~edges of the range swath of SAR images because the incidence angle dependence could not be normalized perfectly. An example of such a failure can be seen along the image boundaries at ~~80N, 35E~~79.5N, 45E in Figure 7 and ~~82.5N, 60E~~79N, 50E in Figure 8, approximately. Third, some artifacts were observed under ~~an extreme marine condition~~large ocean swells. In the classified results in the bottom right panel of Figure 8, there is a misclassified ~~FYI~~ first-year ice patch (yellow) in the open water area. According to the high resolution sea surface winds data from SAR on the Sentinel-1 satellites (https://data.nodc.noaa.gov/cgi-bin/iso?id=gov.noaa.nodc:SAR-WINDS-S1)~~NOAA SAR wind image service, ANSWRS 2.0~~, the wind speed ranged from 17 to 21 m/s at the time of image acquisition heavily roughing the water surface. Although we have included images with both high and low wind conditions in our training data, the image textures of wind roughened water surface and ice were confused in some cases, and the same happened in the image textures of calm water surface and smooth level ice.

**[page 13, lines 1-6]**

was feasible in summer season. The main technological innovation is two-fold: i) minimized manual work in the preparation of training and validation reference data and ii) more objective evaluation of the SAR-based sea ice type classifier compared to the previous studies conducted with small number of images and customized ice type references from informal sources. A conventional approach for selecting training/testing data by anonymous human ice expert is undesirable not only because it is laborious, but also due to subjectivity and lack of standardization in the assessment of the automated classifier. Therefore, the performance from different literature sources cannot be intercompared directly.

## Specific comments

- page 2: line 18, What evidence is there that previous studies were less generalizable than the current one? This statement should be backed up.
  Corrected.

- page 2: line 22, Public ice charts are generated manually. I don't see how using them to train a classifier enables automation.
  The review is right. “enabling automation” was deleted.

- page 3: line 25: objective identification → I assume what the authors are referring to is the way that a large quantity of training labels are pulled from the charts objectively? As compared to manually. Please make this more clear.
  Corrected.

- page 7: line 33: The method is semi-automated in part because of the way the samples are generated, but also because of the use of manually generated ice charts as training data.
  Generation of the reference ice chart is not a part of this algorithm. Our algorithm uses the already exist ice charts made by credible ice experts who are not involved in this study.

- page 11: lines 5-6: `This is because day of year might not correspond to the same temperature...' - Might be better stated `because SAR image features, which partially reflect temperature fluxes and weather regimes, might not correspond to day of year.
  Corrected.

- page 11: line 8: Please refer to the figure number.
  Corrected.

- Figure 8: there are clearly some problems regarding wind roughened water (misclassifications in Fig 8) - The authors acknowledge this, but don't suggest a future path to resolve this issue. There is also some water identified in what might be ice cover in this same figure.
  Added explanations.

English language (not an exhaustive list):

- abstract: line 18, dataset → datasets
  Corrected.
- page 1: line 7, is impacting seriously → can seriously impact
  Corrected.
- page 2: line12, statistics thus → statistics, and thus
  Corrected.
- page 2: line 14: works → studies
  Corrected.
- page 3: line 9: images from the first year is → images from the first year are
  Corrected.
- page 3: line10: is used for validation → are used for validation
  Corrected.
- page 3: line 22: each steps → each step
  Corrected.
- page 6: each polarization images → each polarization image
  Corrected.
- page 6: 'In the literatures about sea ice classification' → Previous studies about sea ice classification
  Corrected.
- page 8: line4, `better recognizable' → 'more easily identified'
  Corrected.
- page 8: line 11 'raters' → rasters
  Corrected.
- page 8: line 11, `trained classifier' → output from the trained classifier
  Corrected.
- page 9: line 32, Do not start a sentence with a Greek letter (please correct at other locations in the manuscript).
  Corrected.
- page 10: line 31, `ices' → ice
  Corrected.
- page 11: line 11: ANSWRS (use of acronym).
  Corrected.

## Anonymous Referee #3

Authors Responses to my major comments are rather disappointing:
Example 1:
My comment: A seasonal assessment of the classification scheme is missing. It the most important issue to address and without this assessment it would not be reasonable to claim the scheme to be either operational or innovative.
Authors Reply: As the reviewer pointed, we did not conduct seasonal assessment. Since the developed algorithm was tested for winter season only, we changed the title as "Classification of Winter Sea Ice Types in Sentinel-1 SAR images"
A similar kind of response also regarding the comments on the usage of ice charts to prepare the training datasets. As I mentioned, I am disappointed with the responses (e.g. A new title, rather than investigating the summer season), but I leave the final decision to the Editor.

First of all, we sincerely apologize for our previous response that made you disappointed. We extended our experiment to assess the performance of the proposed scheme in summer.

As a summary of the new experiment (summer),

- Even the three-class classifier (open water, mixed first-year ice, and old ice) failed to classify different ice types properly. The classification accuracies for old ice were higher than 90% while those for mixed first-year ice were 11-26% with different sets of feature configuration. The accuracy for open water was very high (up to 99%).
- The misclassification between mixed first-year ice and old ice was among themselves.
- These imply that the trained classifier acts like an ice-water discriminator rather than ice type classifier.

The low accuracy for mixed first-year ice might be because of the surface melting and the corresponding image textures which makes the discrimination between the mixed first-year ice and old ice difficult. Another reason might be related to the limitation of the use of microwave region. We compared the output of our three-class classifiers against the OSI SAF sea ice type product, OSI-403-c, in winter season (OSI-403-c does not provide ice types in summer season) and the result was similar to those in the summary with bullet points above. What interesting is, the extent of old ice (multi-year ice) is considerably narrow in OSI-403-c compared to that in NIC ice chart. As the OSI-403-c was produced from microwave observations only (passive microwave radiometers and radar scatterometer), the characteristics of the observed signals may have similarity to those from SAR.

We hope that your concern about the seasonal assessment will be cleared after reading our responses and modifications made to the manuscript. Please find below our modifications (deleted in red and added in blue).

**[page 1, lines 19-24]**

Test results from the ~~datasets~~ dataset spanning ~~two winter seasons~~winter (Jan-Mar) and summer (Jun-Aug) seasons acquired over the Fram Strait and the Barents Sea showed that the classifier is capable of retrieving three generalized cover types (open water, mixed first-year ice, old ice) with ~~an~~ overall ~~accuracy~~ accuracies of ~~85%~~87% and 67% in winter and summer seasons, respectively. For summer season, the classifier performed rather like an ice-water discriminator with high accuracy of 98% as the misclassification between the mixed first-year ice and old was among themselves. ~~and~~ The accuracy for five cover types (open water, new ice, young ice, first-year ice, old ice) in winter season was 60%. ~~with an accuracy of 58%.~~ The errors are

**[page 3, lines 12-16]**

Sentinel-1 TOPSAR data in Extended Wide-swath (EW) mode acquired in ~~two winter seasons (Dec. 2017 – Mar. 2018 and Dec. 2018 – Mar. 2019)~~ summer (June-August in 2016-2018) and winter (January-March in 2017-2019) seasons were collected from the Copernicus Open Access Hub (https://scihub.copernicus.eu). The number of daily image acquisitions covering the study area ranges from 6 to 10 depending on the orbits. The images from the first two years (hereafter called ~~2018 data~~DS1) are used to train the classifier and those from the second year (hereafter called ~~2019 data~~DS2) are used for validation.

**[page 9, lines 3-7]**

phase. Among ~~958~~ 4485 images in total, we selected ~~57~~ 840 images (419 for winter season and 421 for summer season) of which ice edges match well with the collocated ice chart. From the selected images, ~~6.4~~120 million samples covering open water and sea ice were divided into training and test dataset. The DS2 was used to evaluate the performance of the trained classifier using temporally independent dataset of 513 images (281 for winter season and 232 for summer season). The distribution of the image acquisition dates prior to the publication of the reference ice chart is shown in Table 2.

**[page 10, lines 28-34] and [page 11, lines 1-2]**

The confusion matrix for testing the trained classifier for summer season with the test dataset (DS1) is shown is in Table 6. As described in Section 2.2.1, the further simplified three-class classification is applied. The accuracies for open water and old ice were higher than 92%; however, the accuracies for mixed first-year ice were only around 15% both in FC1 and FC2, and 42% in FC3. The large difference between the results of FC1-FC2 and FC3 indicates that the mixed first-year ice likely changes at short time scales. The misclassifications for mixed first-year ice were mostly into old ice. This might be because of the surface melting and the corresponding image textures which makes the discrimination between the mixed first-year ice and old ice difficult. The same patterns were observed from the confusion matrix (Table 7) for validation results from the DS2.

Based on these results, the trained classifiers in summer season are close to ice-water discriminators rather than ice type classifiers.

**[page 11, lines 13-15]**

Figure 9 and 10 show the same mosaics for the case in the summer season. As shown in Table 6 and 7, the misclassifications for the mixed first-year ice into old ice are pronounced in the large ice patches north to Svalbard, while the ice edge positions of the ice chart and the classification result are in well agreement with each other.

**[page 11, lines 32-34] and [page 12, lines 1-14]**

Unfortunately, we could not find an official report regarding the accuracy of the NIC ice chart information. It might be not enough to assess the quality of the classifier output when it is trained with, and evaluated against, only NIC ice charts. The accuracy could be indirectly investigated by comparing the output from our classifier against another data source, such as OSI

SAF sea ice type product (OSI-403-c). The ice classes of OSI-403-c are assigned from atmospherically corrected brightness temperatures of passive microwave radiometers (SSMIS and AMSR2) and backscatter values of radar scatterometer (ASCAT), using a Bayesian approach (Aaboe et al., 2018). Table 10 shows the confusion matrices for our three-class classifiers when their prediction results are compared with the OSI-403-c product as reference. Comparing with the results in Table 9, the accuracies for open water decreased from by 6%; however, this is mainly because the ice concentration threshold for ice-water discrimination in OSI-403-c is 35% which is higher than 20% that we set in our preprocessing of NIC ice chart (Section 2.2.1), thus areas with low ice concentration in marginal ice zone are most likely annotated as open water in OSI-403-c. For first-year ice, large portions (72%) are misclassified as old ice. This might be partly explained from the Figure 12, which shows the ice classes in NIC ice chart and OSI-403-c for the same publication date. A large extent of old ice in NIC ice chart is annotated as multi-year ice in OSI-403-c. As our classifiers were trained with NIC ice chart, it is natural to result in more old ice for the area where the ice type is classified as first-year ice in OSI-403-c. For old ice, the accuracy was the highest, 98%. Finding the reason for the clear discrepancy of the extent of first-year ice between the NIC ice chart and OSI-403-c is beyond the scope of this study, however, it should be noted that an elaborate future work for cross calibrating ice types in different ice charts are necessary.

**[page 11, lines 32-34] and [page 12, lines 1-14]**

## 4 Conclusion

A new semi-automated SAR-based sea ice type classification scheme was proposed in this study. For the first time several ice types ~~can be~~were successfully identified on Sentinel-1 SAR imagery in winter season, while only an ice-water discrimination was feasible in summer season. The main technological innovation is two-fold: i) minimized manual work in the preparation of training and validation reference data and ii) more objective evaluation of the SAR-based sea ice type classifier compared to the previous studies conducted with small number of images and customized ice type references from informal sources. A conventional approach for selecting training/testing data by anonymous human ice expert is undesirable not only because it is laborious, but also due to subjectivity and lack of standardization in the assessment of the automated classifier. Therefore, the performance from different literature sources cannot be intercompared directly.

Test results from the datasets of ~~two winter seasons~~winter season acquired over the Fram Strait and the Barents Sea area showed overall accuracies of ~~85% and 58%~~87% and 60% and the Cohen's kappa coefficients ~~κ~~ of ~~0.80 and 0.67~~0.75 and 0.67 for the three-class and five-class ice type classifiers, respectively. These are slightly lower than the numbers in the previous studies, and the errors are attributed not only to the automated algorithm but also to the inconsistency of the ice charts and the high level of their generalization. Test results from the datasets of summer seasons showed overall accuracy of 67% and the Cohen's kappa coefficient of 0.78 for the three-class classifiers. Considering the misclassifications in different ice types were among themselves, the three-class classifiers performed well at least as an ice-water discriminator with accuracy of 98%.

Based on the results, we envisage that three-class ice type classification from SAR imagery would be useful for making a global sea ice type product like ~~EUMETSAT OSI-403-C~~OSI SAF OSI-403-c with higher spatial resolution. The proposed approach importantly showed that a daily ice type mapping from the Sentinel-1 data is feasible and can help capture details of short-term changes in the stage of sea ice development. Based on the achieved results, we believe that the proposed approach may be efficiently used for operational ice charting services for supporting navigation in the Arctic.

**[Figure 4]**

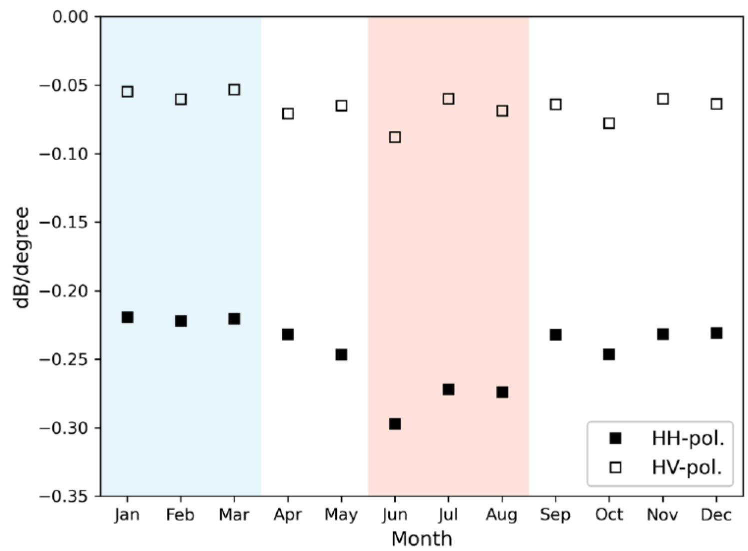


**Figure 4: Incidence angle dependences of sigma naught in HH (closed squares) and HV (open squares) polarization channels. Pixels covering various types of sea ice were merged so that the averaged property can be estimated. The blue and red zones indicate winter and summer seasons, respectively.**

[Figure 9]

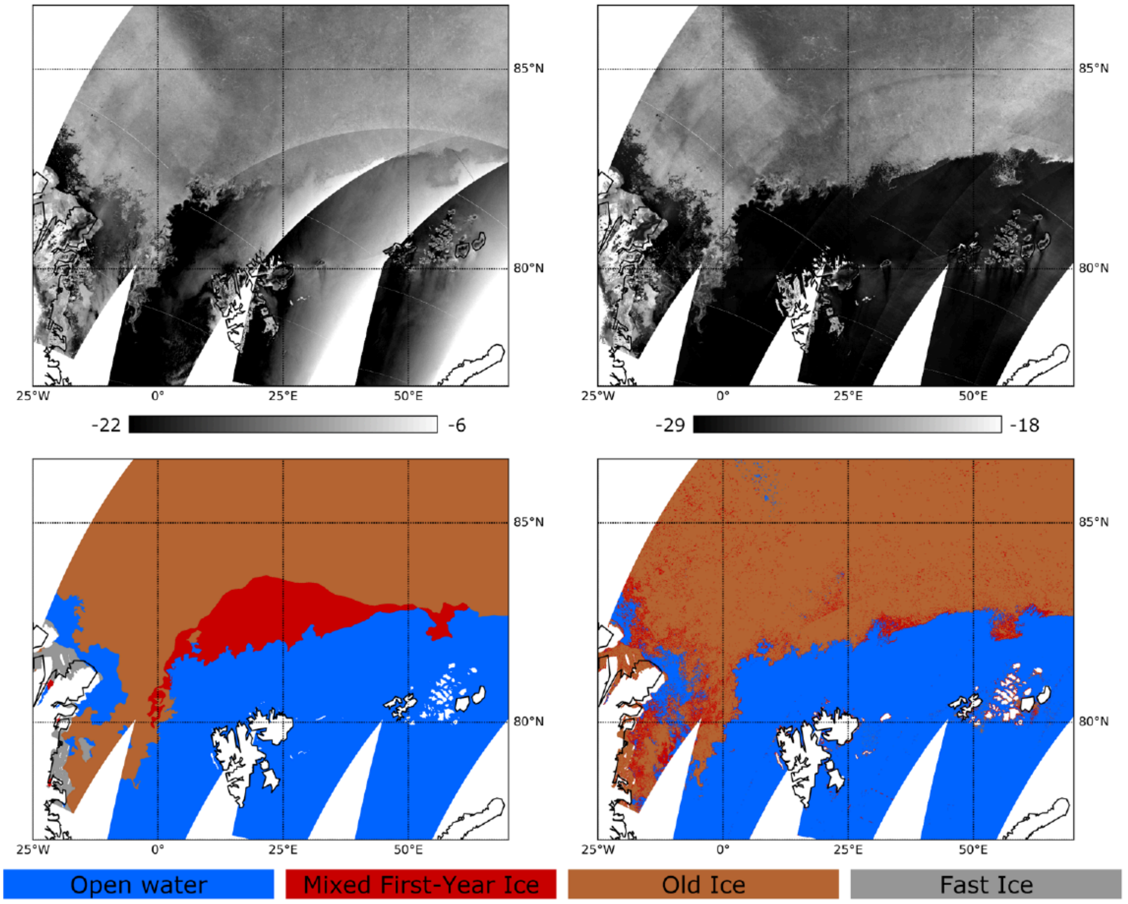


Figure 9: One-day mosaics of Sentinel-1A/1B images (Top left: HH, Top right: HV) and the ice classification result (Bottom right) on 13 August 2018. The publication date of the reference weekly ice chart is 16 August 2018 (Bottom left).

**[Figure 10]**

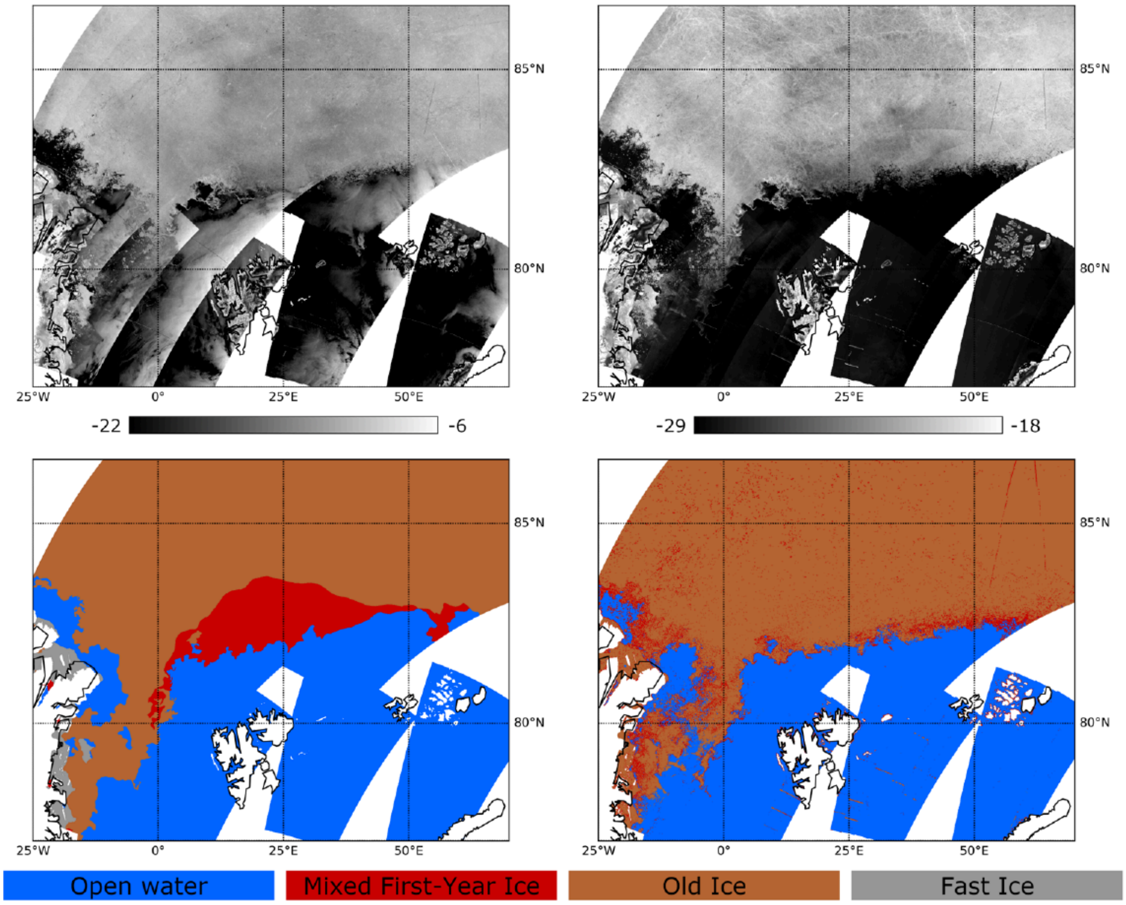


Figure 10: One-day mosaics of Sentinel-1A/1B images (Top left: HH, Top right: HV) and the ice classification result (Bottom right) on 16 August 2018. The publication date of the reference weekly ice chart is 16 August 2018 (Bottom left).

**[Figure 12]**

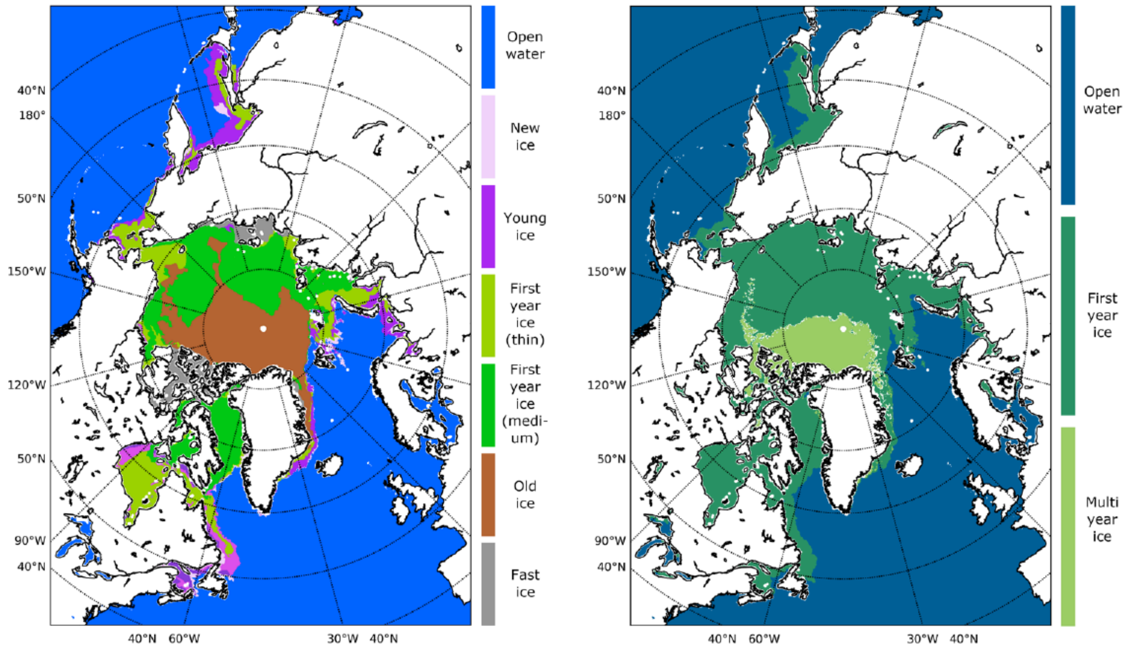


Figure 12: The ice types in NIC ice chart (left) and OSI SAF sea ice type product (right) for the same date (8 Jan. 2019). Note that the SoD labels and colors follows those defined in each ice chart format.

**[Table 6] and [Table 7]**

**Table 6: Confusion matrix of the three-class RF classifier which was trained with and applied to the DS1 summer dataset**

| | | Predicted | | | | | | | | |
|---|---|---|---|---|---|---|---|---|---|---|
| | | OW (open water) | | | mFYI (mixed first-year ice) | | | OI (old ice) | | |
| | Case | FC1 | FC2 | FC3 | FC1 | FC2 | FC3 | FC1 | FC2 | FC3 |
| Actual | OW | **98.1** | **97.9** | **98.7** | 0.7 | 0.7 | 0.6 | 1.2 | 1.4 | 0.6 |
| | mFYI | 4.1 | 3.9 | 2.4 | **14.9** | **15.5** | **41.8** | 81.1 | 80.6 | 55.8 |
| | OI | 1.5 | 1.4 | 1.0 | 5.5 | 5.7 | 4.9 | **93.0** | **92.9** | **94.1** |

**Table 7: Confusion matrix of the three-class RF classifier which was trained with DS1 summer dataset and applied to the DS2 summer dataset**

| | | Predicted | | | | | | | | |
|---|---|---|---|---|---|---|---|---|---|---|
| | | OW (open water) | | | mFYI (mixed first-year ice) | | | OI (old ice) | | |
| | Case | FC1 | FC2 | FC3 | FC1 | FC2 | FC3 | FC1 | FC2 | FC3 |
| Actual | OW | **99.5** | **99.4** | **96.2** | 0.2 | 0.2 | 3.2 | 0.3 | 0.4 | 0.6 |
| | mFYI | 5.4 | 5.1 | 3.0 | **12.0** | **11.2** | **25.8** | 82.5 | 83.7 | 71.2 |
| | OI | 2.9 | 2.7 | 2.2 | 5.8 | 5.8 | 13.4 | **91.2** | **91.4** | **84.4** |

**[Table 10]**

**Table 10: Confusion matrix of the three-class RF classifier which was trained with DS1 winter dataset and applied to the DS2 winter dataset with reference to OSI SAF sea ice type product (OSI-403-c)**

| | | Predicted (classifier was trained with NIC ice chart) | | | | | | | | |
|---|---|---|---|---|---|---|---|---|---|---|
| | | Open water | | | Mixed first-year ice | | | Old ice | | |
| | Case | FC1 | FC2 | FC3 | FC1 | FC2 | FC3 | FC1 | FC2 | FC3 |
| Reference (OSI SAF) | Open water | **85.9** | **86.1** | **86.2** | 12.6 | 12.4 | 12.1 | 15.7 | 15.3 | 16.2 |
| | First-year ice | 1.9 | 1.6 | 2.0 | **26.0** | **26.8** | **26.9** | 72.1 | 71.6 | 71.2 |
| | Multi-year ice | 0.1 | 0.1 | 0.1 | 1.5 | 1.4 | 1.4 | **98.4** | **98.5** | **98.5** |

# Classification of ~~Winter~~ Sea Ice Types in Sentinel-1 SAR images

Jeong-Won Park[1,2], Anton A. Korosov[1], Mohamed Babiker[1], Joong-Sun Won[3], Morten W. Hansen[1,4], Hyun-cheol Kim[2]

[1]Ocean and Sea Ice Remote Sensing Group, Nansen Environmental and Remote Sensing Center, Bergen, 5006, Norway
[2]Unit of Arctic Sea Ice Prediction, Korea Polar Research Institute, Incheon, 21990, South Korea
[3]Department of Earth System Sciences, Yonsei University, Seoul, 03722, South Korea
[4]Department of Remote Sensing and Data Management, Norwegian Meteorolotical Institute, 0371 Oslo, Norway

*Correspondence to*: Jeong-Won Park (jeong-won.park@kopri.re.kr)

**Abstract.** A new Sentinel-1 image-based sea ice classification algorithm using a machine learning-based model trained in a semi-automated manner is proposed to support daily ice charting. Previous studies mostly rely on manual work in selecting training and validation data. We show that the readily available ice charts from the operational ice services can reduce the ~~number~~ amount of manual works in preparation of large amounts of training/testing data. Furthermore, they reduce the inconsistent decisions in the classification algorithm by indirectly exploiting the best ability of the sea ice experts working at the operational ice services. The proposed scheme has two phases: training and operational. Both phases start from the removal of thermal, scalloping, and textural noise from Sentinel-1 data and calculation of gray level co-occurrence matrix and Haralick texture features in a sliding window. In the training phase, the weekly ice charts are reprojected into the SAR image geometry. A random forest classifier is trained with the texture features on input and labels from the rasterized ice charts on output. Then, the trained classifier is directly applied to the texture features from Sentinel-1 images ~~in an operational manner~~operationally. Test results from the ~~datasets~~ dataset spanning ~~two winter seasons~~winter (Jan-Mar) and summer (Jun-Aug) seasons acquired over the Fram Strait and the Barents Sea showed that the classifier is capable of retrieving three generalized cover types (open water, mixed first-year ice, old ice) with ~~an~~ overall ~~accuracy~~ accuracies of ~~85%~~87% and 67% in winter and summer seasons, respectively. For summer season, the classifier performed rather like an ice-water discriminator with high accuracy of 98% as the misclassification between the mixed first-year ice and old was among themselves. ~~and~~ The accuracy for five cover types (open water, new ice, young ice, first-year ice, old ice) in winter season was 60%. ~~with an accuracy of 58%.~~ The errors are attributed both to incorrect manual classification on the ice charts and to the semi-automated algorithm. Finally, we demonstrate the potential for near-real time service of the ice map using daily mosaiced Sentinel-1 images.

## 1 Introduction

Wide swath SAR observation from several spaceborne SAR missions (RADARSAT-1, 1995-2013; Envisat ASAR, 2002-2012; ALOS-1 PALSAR, 2006-2011; RADARSAT-2, 2007-present; Sentinel-1, 2014-present) played an important role in studying global ocean and ice-covered Polar Regions. The Sentinel-1 constellation (1A and 1B) is producing dual-polarization observation data with the largest Arctic coverage and the highest temporal resolution ever. The cross-polarization is known to be more sensitive to the difference in scattering from sea ice and open water than the co-polarization (Scheuchl et al., 2004), and the combination of HH- and HV-polarizations has been widely used for ice edge detection and ice type classification (a nice overview is given in the paper by Zakhvatkina et al., 2019). However, most of the recent ice classification algorithms were developed using RADARSAT-2 ScanSAR (Leigh et al., 2014; Liu et al., 2015; Zakhvatkina et al., 2017) which has different sensor characteristics from Sentinel-1 TOPSAR, and the use of Sentinel-1 for the same purpose is very limited in literature. The main drawback of applying existing algorithms to Sentinel-1 TOPSAR data is the relatively high level of thermal noise contamination and its propagation to image textures.

For proper use of dense time-series of Earth observations using SAR sensors, radiometric properties must be well-calibrated. Thermal noise is often neglected in many cases, but ~~is impacting seriously~~ can seriously impact the utility of dual-polarization SAR data. Sentinel-1 TOPSAR image intensity is particularly disturbed by the thermal noise in the cross-polarization channel. Although the European Space Agency (ESA) provides calibrated noise vectors for noise power subtraction, residual noise contribution is still significant considering the relatively narrow backscattering distribution of the cross-polarization channel. In our previous study (Park et al. 2018), a new denoising method with azimuth de-scalloping, noise scaling, and inter-swath power balancing was developed and showed improved performance in various SAR intensity-based applications. Furthermore, when it came to texture-based image classification, we suggested a correction method for textural noise (Park et al., 2019) which distorts local statistics, and thus degrades texture information in the Sentinel-1 TOPSAR images.

In many of the previous ~~works~~ studies on ice-water and/or sea ice classification (Soh and Tsatsoulis, 1999; Zakhvatkina et al., 2013; Leigh et al., 2014; Liu et al., 2015; Ressel et al., 2015; Zakhvatkina et al., 2017; Aldenhoff et al., 2018), the training and validation were done using manually produced ice maps. Although the authors claimed that the manual ice maps were drawn by ice experts, the selection of SAR scenes and interpretation ~~can~~ could be inconsistent, and the number of samples ~~was~~ might not be enough to generalize the results because of the laborious manual work. Furthermore, the results are hardly reproducible by others because the reference sources are not open to public. Therefore, increasing objectivity is crucial, and automating the classification process is encouraged. The idea of training using SAR images and accompanying image analysis charts, which is a raw interpretation of SAR images by trained ice analysts working at operational ice services, were tested for sea ice concentration estimation by Wang et al. (2017); however, such image analysis charts are not accessible to the public.

The use of a public ice chart as training and validation reference data may help in solving the validation problem ~~and enabling automation~~. The preparation of a public ice chart is also through manual inspection of various sources of satellite imagery and other sources of data (Partington et al., 2003; Johannessen et al., 2006); however, training using a large volume of these charts would reduce operator-to-operator bias, such as inconsistent decisions against similar ice conditions. The overall bias may exist since the public ice charts are produced in the interest of marine safety. Nevertheless, as the human interpretation available in the ice chart is currently considered as the best available information of sea ice (Karvonen et al., 2015), the best practice to make a sea ice type classifier is to train with the public ice chart so that the best knowledge of certified ice analysts is mimicked.

In this work, we present a semi-automated Sentinel-1 image-based sea ice classification algorithm which takes advantage of our denoising method. The noise corrected dual-polarization images are processed into image textures that capture sea ice features in various spatial scales, and they are used for supervised classification with a random forest classifier by relating with ice charts published by operational ice services. The use of ice charts has dual purposes: semi-automatization of classifier training, and minimization of human error.

## 2 Data and methods

### 2.1 Study area and used data

The region of study for developing and testing the proposed algorithm is the Fram Strait and the Barents Sea including a part of the Arctic Ocean (10ºW-70ºE, 75ºN-85ºN) as shown in Figure 1. Various sea ice types are found in this area due to the intensive export of multi-year ice through the Fram Strait (Smedsrud et al., 2017), and development of young and first-year ice between Svalbard and Franz Josef Land.

Sentinel-1 TOPSAR data in Extended Wide-swath (EW) mode acquired in ~~two winter seasons (Dec. 2017 – Mar. 2018 and Dec. 2018 – Mar. 2019)~~ summer (June-August in 2016-2018) and winter (January-March in 2017-2019) seasons were collected from the Copernicus Open Access Hub (https://scihub.copernicus.eu). The number of daily image acquisitions covering the study area ranges from 6 to 10 depending on the orbits. The images from the first two years (hereafter called ~~2018 data~~DS1) are used to train the classifier and those from the ~~second~~ third year (hereafter called ~~2019 data~~DS2) are used for validation.

The ice charts covering the same periods were collected. There are two ice services that publish weekly ice charts with Pan-Arctic coverage: U. S. National Ice Center (NIC) of the United States of America, and Arctic and Antarctic Research Institute (AARI) of Russia. Although the accuracies are known to be comparable (Pastusiak, 2016) to each other, there is no partial ice concentration information in the AARI ice chart. In this study, we use the ice charts downloaded from the NIC website (https://www.natice.noaa.gov/Main_Products.htm).

### 2.2 Methods

Figure 2 shows the flow of the semi-automated ice classification scheme that we propose. It is divided into two phases: training and operational. Both phases start from the removal of thermal noise from Sentinel-1 data (Section 2.2.2), incidence angle calibration (Section 2.2.3), and calculating texture features (Section 2.2.4). The training phase (shown in gray in Figure 2) continues with preprocessing and collocation of the ice charts with the Sentinel-1 data (Section 2.2.1) and machine learning step (Section 2.2.5 and 2.2.6). The operational phase uses the classifier of which developed during the training phase for processing texture features that were computed from the input SAR data and for generating ice charts. Detailed explanations for each step are given in the following subsections.

### 2.2.1 Ice chart preprocessing

To take advantage of the objective identification of the ice type from credible sources and to develop a semi-automated processing scheme, the proposed algorithm uses electronic ice charts published by international ice chart services. The electronic ice chart follows SIGRID-3 format (JCOMM, 2014a), which is based on a vector format called shapefile (ESRI, 1998). The first step is to reproject the ice chart into the geometry of each SAR image. Although an accurate reprojection needs several pieces of information such as orbit, look angle, topographic height, etc., our interest is in the sea ice where the topographic difference does not exceed more than few meters, hence the reprojection of coordinates of ice chart polygons is done with Geospatial Data Abstraction Library (GDAL; GDAL/OGR contributors, 2019) using a simple 3rd order polynomial fitted using the ground control points information from the Sentinel-1 product-included auxiliary data.

After the reprojection, the following three layers are extracted: total ice concentration (CT), partial ice concentration of each ice type (CP), and stage of development (SoD). CT is important because areas with low CT can be misinterpreted as open ocean in a SAR image. Heinrichs et al. (2006) reported that the ice edge determined from AMSR-E passive microwave radiometer data using the isoline of 15% concentration matches best the ice edge determined from RADARSAT-1 SAR data using visual inspection. After the visual comparison of many SAR images and the corresponding reprojected ice charts, we set a threshold of 20% for CT to discard water-like pixels. Note that the ice concentration label in the SIGRID-3 format is assigned in an increment of 10%. CP is also important in finding the dominant ice type in the given polygons. SoD is a so-called ice type. It is challenging to differentiate ice types using SAR data only, thus we merged the SoDs into simple five classes: open water, new ice, young ice, first-year ice, and old ice. For summer season (Jun-Aug), there is almost no new ice and young ice annotated in the NIC ice chart, the SoDs are further merged into three classes: open water, mixed first-year ice, and old ice.

Figure 3 demonstrates an example of the ice chart preprocessing explained above with the colors following the WMO nomenclature (JCOMM, 2014b). Comparing the original SoD in the top left panel with the processed SoD in the bottom left panel, it is clear that the ice edge of the processed SoD match better with the SAR backscattering images.

### 2.2.2 Denoising of Sentinel-1 imagery

Sentinel-1 cross-polarization images suffer from strong noise ~~of which are originated~~, some which originate from combined effects of the relatively low signal-to-noise ratio of the sensor system and insufficient noise vector information in the Extra Wide-swath mode Level-1 product (Park et al., 2018). For surfaces with low backscattering such as calm open water and level sea ice without the presence of frost flowers on top, the effects from thermal noise contamination are visible not only in the backscattering image but also in some of the texture images (Park et al., 2019). The authors have developed an efficient method for textural denoising which is essential for the preprocessing of Sentinel-1 TOPSAR dual polarization products. Denoising ensures beam-normalized texture properties for all subswaths, which helps seamless mosaic of multi-pass images regardless of the satellite orbit and image acquisition geometry. By following the methods developed in Park et al. (2018, 2019), each of the Sentinel-1 images was denoised before further processes are applied. As the noise power subtraction yields negative intensity values where the backscattering power is close to the noise floor, especially in HV polarization, we added mean of the noise power back to the denoised result so that those pixels do not turn into NaN (not a number) by the sigma naught conversion of linear scale to log scale (decibel).

### 2.2.3 Incidence angle correction

It is well known that there is a strong incidence angle dependence in the SAR backscattering intensity for open water and sea ice surface (Mäkynen et al., 2002; Mäkynen and Karvonen, 2017). For wide-swath SAR system like Sentinel-1 TOPSAR, varying backscatter intensity confuses image interpretation. The quasi-linear slopes in the plane of incidence angle versus sigma nought in decibel scale for typical first-year ice are reported as -0.24 and -0.16 dB/degree for HH- and HV-polarization, respectively (Mäkynen and Karvonen, 2017). To normalize the backscattering intensity for all swath range, these slopes were compensated for or used as input layer in several ice classification algorithms in the literature (Liu et al., 2015; Zakhvatkina et al., 2013, 2017; Karvonen, 2014, 2017; Aldenhoff et al., 2018). Although the angular dependency is not a system-dependent variable but is governed by physical characteristics of the backscattered surface, the numbers need to be reassessed because the estimations of Mäkynen and Karvonen (2017) might have been affected by the residual thermal noise which used to be very strong before the ESA has updated the noise removal scheme in 2018 (Miranda, 2018).

~~Figure 4 shows two-dimensional histograms of incidence angle versus sigma nought for sea ice pixels in HH and HV polarization channels from Sentinel-1 data collected over sea ice and open water in the study area in winter 2018.~~ Figure 4 shows incidence angle dependence in the SAR backscattering intensity for mixed sea ice types. From the Sentinel-1 dataset described in Section 2.1, sea ice pixels were extracted by using daily global sea ice edge products available from the EUMETSAT Ocean and Sea Ice Satellite Application Facilities (OSI SAF). For mid-winter season (Jan-Mar displayed by blue background), ~~For HH polarization,~~ the estimated mean slope in HH polarization was ~~-0.200~~-0.21 dB/degree, which is slightly different from the estimation of the first-year ice (-0.24 dB/degree) in Mäkynen and Karvonen (2017) and in between the estimations for first-year ice (-0.22 dB/degree) and multi-year ice (-0.16 dB/degree) in Mahmud et al. (2018). For HV polarization, the estimated slope was only ~~-0.025~~-0.06 dB/degree, which is much lower than ~~the estimation~~-0.16 dB/degree for deformed first-year ice in Mäkynen and Karvonen (2017), however, it is in line with the estimations ~~from RADARSAT-2 (Leigh et al., 2014; Liu et al., 2015).~~in Liu et al., 2015. Work by Leigh et al. (2014) stated that the HV polarization backscatter signatures are largely unaffected by incidence angle variation in their RADARSAT-2 dataset. For summer season (Jun-Aug displayed by red background), the mean slopes increased to -0.28 and -0.08 dB/degree in HH and HV polarization, respectively. Scharien et al. (2014) reported significant slopes for ice adjacent to melt ponds in June, and Gill et al. (2015) also found slopes of -0.33 and -0.25 for smooth first-year ice in May in HH and HV polarization, respectively. The smaller slopes in our estimation are likely due to the mixed ice types and structures; the SAR backscattering of deformed ice has lower incidence angle dependency as shown in Mäkynen and Karvonen (2017).

We compensate for the incidence angle dependence using the estimated slopes with respect to the nominal scene center angle of 34.5 degrees as reference. Although the incidence angle dependence changes with ice type and radar frequency (Mahmud et al., 2018), the compensation is done for all pixels in the image using a single value of mean slope because the ice types are not identified in this stage. Open water areas of the image are also affected; however, the correction is also beneficial since the incidence angle dependence for open water is stronger (-0.65 dB/degree for wind velocity of 5 m/s, computed from CMOD5 C-band geophysical model function in Hersbach et al., 2007), thus the corrected image has less incidence angle dependence.

### 2.2.4 Texture feature computation

Like many of the previously developed sea ice type classification methods (Shokr, 1991; Barber and LeDrew, 1991; Soh and Tsatsoulis, 1999; Deng and Clausi, 2005; Zakhvatkina et al., 2013; Leigh et al., 2014; Liu et al., 2015), the proposed approach starts from gray level co-occurrence matrices (GLCM) calculation. The GLCM is a four-dimensional matrix $P(i, j, d, a)$ calculated from two grey tones of reference pixel $i$, and its neighbor $j$, with co-occurrence distance $d$, and orientation $a$. Haralick et al. (1973) have introduced a set of GLCM-based texture features called Haralick features, and its practicality has been reported in numerous research. Since 13 Haralick features can be calculated for each of the two-dimensional slices $P(i, j)$ for multiple $d$ and $a$, the maximum number of texture features is to be as $2 \times 13 \times d \times a = 26da$, where 2 is for accounting dual polarization. It is common to take the directional average for 0°, 45°, 90°, and 135° to reduce GLCM dimensionality. Further averaging for multiple distances (1 to $w/2$ where $w$ is the size of subwindow for GLCM computation) is taken after computing normalized GLCM. The spatial resolution of the texture features is the pixel spacing of Sentinel-1 EW-mode GRDM image (40 m) multiplied by $w$. In this study, we set $w$ as 25 so that the grid spacing of the result of texture analysis is 1 km.

An important factor that influences the computed texture features is the number of gray levels, $L$. Considering the radiometric stability of Sentinel-1 EW mode (0.32 dB; Miranda, 2018) and the range of sigma nought for various ice types (-31 to 0 dB for HH, -32 to -7 dB for HV; estimated from ~~Figure 4~~DS1 and DS2 after incidence angle correction), the number of gray level should be sufficiently large enough to capture their actual differences in sigma nought values. The optimal quantization level can be calculated using the ratio of sigma nought range to radiometric resolution as follows:

For HH, $$\frac{(0\ dB)-(-31\ dB)}{0.32\ dB} = 96.875 \quad (1)$$

For HV, $$\frac{(-7\ dB)-(-32\ dB)}{0.32\ dB} = 78.125 \quad (2)$$

Since $L$ should be sufficiently large to take the full advantage of system capability and yet, the computation cost should not be too expensive, in this study, we set $L$ as 64, which is the closest power of 2 to the resulting numbers from the equations above. In addition to 13 Haralick features, the coefficient of variation (CV) which is reported as a useful feature for ice-water discrimination (Keller et al., 2017) is included. The CV is defined as follows:

$$CV = \sigma/\mu \quad (3)$$

where $\sigma$ and $\mu$ are the standard deviation and mean of the samples in a given subwindow. Since CV can be computed for each polarization ~~images~~image, the number of texture features for Sentinel-1 dual-polarization data is extended to 28. Incidence angle and day-of-the-year can also be added. The former is adopted to account for possible residuals from the angular dependency correction while the latter is to account for seasonal variability. Although these two are not any type of textures, they can be used as input features for image classification. Note that it is important to have each ice type spatially and temporally even distributions if these two additional features are included; otherwise, the trained classifier will result a biased prediction. The effects of including these extra features will be tested and discussed in later sections.

**2.2.5 Machine learning classifier**

Since there are hundreds of algorithms in the field of machine learning (ML) and each of the different algorithms has its own pros and cons, it is not easy to compare their performances and decide what to use. Fernández-Delgado et al. (2014) evaluated that the Random Forest (RF; Ho, 1998) was the best classifier for various types of datasets with slight difference from Support Vector Machine (SVM; Cortes and Vapnik, 1995). In the ~~literatures~~ previous studies about sea ice classification (e.g., Leigh et al., 2014; Liu et al., 2015; Zakhvatkina et al., 2017), the SVM was used often because by nature it works relatively well even when the number of datasets are small. When training dataset is prepared by manual work (i.e., manual classification by human expert), the number of images is not large, usually less than 20 (e.g., 12 scenes in Zakhvatkina et al., 2013; 20 scenes in Leigh et al., 2013; ~~2 scenes~~1 scene in Liu et al., 2015; 4 scenes in Ressel et al., 2015). However, the number can increase with less effort when the readily available ice charts are used as training references. Besides, there is no need to rely on additional manual work prone to contamination by biased decisions. The RF has two practical advantages when processing a large number of datasets. First, the RF is scale-invariant and does not require preprocessing of the datasets whereas the SVM requires scaling and normalization. Second, the computational complexity of the RF is lower than that of the SVM. For the SVM, the number of operations is $O(n^2p + n^3)$ and $O(n_{sv}p)$ for training and prediction while for RF, $O(n^2pn_{tr})$ and $O(n_{tr}p)$, respectively, where $n$ is the number of samples, $p$ is the number of features, $n_{sv}$ for the number of support vectors, and $n_{tr}$ for the number of trees. Considering the practical requirements of fast processing for near-real time ice charting services, the RF can be a reasonable solution. We use the RF with the Python Scikit-Learn implementation (Pedregosa et al., 2011).

We split the RF classifier into several binary classifiers using a one-vs-all scheme (Anand et al., 1995). Although the standard RF algorithm can inherently deal with a multiclass problem, the one-vs-all binarization to the RF results in better accuracy with smaller forest sizes than the standard RF (Adnan and Islam, 2015).

Three hyperparameters of the RF classifier were tuned: number of trees ($N_T$), maximum tree depth ($D$), and maximum number of features ($N_F$). Usually, with the higher $N_T$ and $D$, the model better fits to the data. However, increasing forest size can slow down the training process considerably, and more importantly, it can cause overfitting. Therefore, it is important to tune these hyperparameters adequately so that the processing time and performance are in balance. To determine the best values of the hyperparameters, a grid search with five-fold cross-validation (Kohavi, 1995) is used. The grid (all possible combinations of $N_T$, $D$, and $N_F$ values) is set in a logarithmic scale (Table 1) because the performance change with hyperparameter is typically in a logarithmic scale. Classification scores with values ranging from 0 (worst performance) to 1 (best performance) are evaluated for each node of the grid and are interpolated between the nodes by curve fitting. The Richards' Curve (Richards, 1959) was used as the fit model because it allows easy estimation of the model's maximum value. The optimal values for $N_T$, $D$, and $N_F$ are selected based on the saturation of score increment, difference between training and testing score, and computational load considerations.

### 2.2.6 Training and validation

To train an ice type classifier, a set of collocated SAR images and ice charts is required. After the preprocessing of the ice chart including reprojection into the SAR image geometry, only the samples with spatially and temporally good matches should be fed to the training phase. The goodness of matching should be examined as the weekly ice chart is produced by merging information from many image sources acquired in different time instances, hence the ice locations and conditions are unlikely match to those in every SAR image. As no explicit scene identifier or time information of the images used in ice charting is provided with the ice chart itself, the basic strategy in image selection is to find a pair of SAR image and ice chart which match well visually. Such an i~~I~~mage selection is trivial, but not easy to automate. Since the weekly ice chart is made partly based on the SAR images acquired in the past three days from the date of publication, the ice edges in some images match well with those in the ice chart.

In order to automate image selection, the ice edges in SAR images need to be identified first. Since even an ice/water classifier has not been well developed yet for Sentinel-1, the image selection procedure has to be done manually in the beginning. However, once a classifier is generated with high accuracy, it can be used to automate the procedure, then the whole process in the proposed scheme will be fully automated. This is why the proposed algorithm is named "semi-" automated for now. Nevertheless, the manual selection to guarantee a "good match" is done by visual inspection of ice-water boundaries overlaid on SAR images. The ice-water boundary can be extracted easily from the reprojected ice chart~~ by selecting the pixel borders of open water class~~. Then the SAR backscattering image contrasts across the ice-water boundaries are examined both in HH- and HV-polarization because the image contrast between ice-water is larger in HV ~~and~~ while smooth level ice is ~~better recognizable~~more easily identified in HH.

After the image selection, the samples in the selected images are split randomly into training and test datasets with a ratio of 7:3. For the training dataset, further data selection is made by excluding the samples residing close to the polygon boundaries. This is to account for possible mismatch due to various reasons (e.g., ice drift, vector mapping error, image geocoding error, etc.). In this study, only the data from pixels more than 3 km away from the polygon boundaries was fed into the training process. Once the hyperparameter optimization is done, the RF classifier is trained for the training dataset. The trained classifier is then applied to the test dataset. For performance evaluation, we use confusion matrix and Cohen's kappa coefficient $\kappa$ (Cohen, 1960), which measures the agreement between two ~~raters~~ rasters (in this study, they are the output from the trained classifier and the reference ice chart) with taking account of the possibility of the agreement occurring by chance. The validation is done in the same way but using a completely independent dataset. The ~~2018 data~~DS1 was used to run the training phase. Among ~~958~~ 4485 images in total, we selected ~~57~~ 840 images (419 for winter season and 421 for summer season) of which ice edges match well with the collocated ice chart. From the selected images, ~~6.4~~120 million samples covering open water and sea ice were divided into training and test dataset. The DS2 was used to evaluate the performance of the trained classifier using temporally independent dataset of 513 images (281 for winter season and 232 for summer season). The distribution of the image acquisition dates prior to the publication of the reference ice chart is shown in Table 2.

**3 Results and discussion**

We trained three RF classifiers with different feature configurations: i) FC1: Haralick texture features and CV, ii) FC2: Haralick texture features, CV, and incidence angle, iii) FC3: Haralick texture features, CV, incidence angle, and day-of-the-year.

As expected, the classification score increases with the number of trees (crosses on Figure 5, upper panel) and Richards' curve (dashed line) fits well to the observations (RMSE=$2.3 \times 10^{-4}$). The optimal $N_T$ value is selected where the score increment per tree (i.e., local slope) becomes less than 0.001 (i.e., accuracy increase of 0.1%) and constitutes 11 trees thus keeping the forest size small. The scores also increase with the maximum tree depth (crosses on Figure 5, middle panel) but Richards' curve (dashed line) doesn't fit so well (RMSE=$3.6 \times 10^{-3}$) and cannot be used for finding the optimal $D$ value. This can be explained by overfitting of the classifier and illustrated by the difference between training and testing scores (Figure 5, lower panel): small difference between the scores (for $D \leq 8$) indicate similar performance on training and testing datasets, while large difference (for $D > 8$) indicate that testing dataset is processed with worse results. The optimal $D$ value is therefore selected where the score difference become higher than 0.03 and constitutes 8 levels. The optimal value of the number of features ($N_F$) was selected using the same criterion as for $N_T$ and the value constitutes 10 features. As a result, the optimal hyperparameters of the number of trees, the maximum tree depth, and the number of features were 11, 8, and 10, respectively. The trained five-class classifier consists of five binary sub-classifiers, each of them is used for discriminating one specific class from the others. For each sub-classifier, each texture feature has a different weight in decision making. The fraction of the samples that each texture feature contributes can be used to compute the relative importance of the features, and the averaged estimates of them over several randomized trees serve as an indicator of feature importance (Louppe, 2014). The feature importance of the sub-classifiers is presented in Figure 6. The overall pattern shows that the features of HV polarization play a more important role than those of HH polarization. For HH polarization, the sum average, which is equal to the mean backscattering intensity in each subwindow, was the prominent feature. For HV polarization, however, contrast, variance- and entropy-related features were more important. The classifiers for open water and old ice have more strong dependencies on HV polarization than others. This is understandable because the main radar scattering mechanisms for those two types are strongly characterized by the portion of volume scattering: low for calm water and high for dry ice with low salinity (old ice).

The classifier for new ice has a distinctive pattern that the sum averages in both polarizations are much more important than other features. This might be because the new ice has different types of recently formed ice including nilas, which is smooth but rafting can make rough features, and frost flowers, which introduces high surface roughness and volume scattering (Isleifson et al., 2014), thus the new ice can appear either featureless dark or complex bright in SAR image (Dierking, 2010). The large range in backscatter values makes it hard to define characteristic texture in the new ice patch.

The confusion matrix for testing the trained classifier for winter season with the test dataset (~~2018 data~~DS1) is shown is in Table ~~2~~3. Three cases with different feature configurations (FC1-FC3) were tested. The accuracies for open water and old ice were higher than ~~85~~90%; however, those for young ice and first-year ice were around 60%. The mean difference between the results of FC1 and FC2 was only ~~1.6%~~1.2%, indicating that residual angular dependency was negligible after the incidence angle correction. However, the accuracy significantly improved from FC2 to FC3, especially with new ice (~~24.5%~~21.2%). The Cohen's kappa coefficient $\kappa$ for FC1, FC2, and FC3 were 0.70, 0.71, and 0.77, respectively. It should be noted that the evaluation of the ~~2018 data~~DS1 was carried out with the input dataset that was used for training. Thus, the test and training data share the same ice conditions as well as spatio-temporal coverage. As a result, the $\kappa$ might contain correlation which is not preferable for proper evaluation. Table ~~3~~ 4 shows the confusion matrix for validation results from the ~~2019 data~~DS2 of which the accuracy of open water and old ice was at a similar level, compared to the ~~2018 data~~DS1. Meanwhile, for the accuracy of ~~new ice,~~ young ice, and first-year ice decreased considerably. The differences between the results of ~~FC1 and FC2~~FC1, FC2, and FC3 were insignificant~~whereas there were notable accuracy degrades from FC2 to FC3~~. This result is opposite to the ~~2018 data~~DS1 inferring that the training with FC3 was overfitted and the day-of-the-year may not correspond to the temperature, air-sea fluxes, or weather regimes. The $\kappa$ for FC1, FC2, and FC3 with the ~~2019 data~~DS2 were 0.67, 0.67, and ~~0.49~~0.67, respectively.

To see how the denoising step in Section 2.2.2 led to improvements in the classification accuracies, the same training and evaluation were conducted for the same dataset without applying the textural noise correction (Table ~~4~~5). In ~~both FC1 and FC2~~all configurations (FC1-FC3), the accuracies improved for young ice (~~+8.2-9.8%~~+2.4-6.2%) and ~~first-year ice (+9.2-11.6%)~~old ice (+3.9-4.5%) which were most pronounced compared to those for open water (~~+1.7%~~+1.1-1.9%) and ~~old ice (+1.2-1.7%)~~first-year ice (-0.2-0.9%). On the contrary, a small accuracy decrease was observed for new ice (~~-2.8-4.7%~~-0.3-2.4%). Nevertheless, the improvement in ~~kappa~~ $\kappa$ (~~+0.05~~+0.08) demonstrates a clear improvement in the overall classification result.

The confusion matrix for testing the trained classifier for summer season with the test dataset (DS1) is shown is in Table 6. As described in Section 2.2.1, the further simplified three-class classification is applied. The accuracies for open water and old ice were higher than 92%; however, the accuracies for mixed first-year ice were only around 15% both in FC1 and FC2, and 42% in FC3. The large difference between the results of FC1-FC2 and FC3 indicates that the mixed first-year ice likely changes at short time scales. The misclassifications for mixed first-year ice were mostly into old ice. This might be because of the surface melting and the corresponding image textures which makes the discrimination between the mixed first-year ice and old ice difficult. The same patterns were observed from the confusion matrix (Table 7) for validation results from the DS2.

Based on these results, the trained classifiers in summer season are close to ice-water discriminators rather than ice type classifiers.

Figure 7 shows a daily mosaic of Sentinel-1 SAR images over the study area and the classified ice map in the winter season. For comparison, the NIC weekly ice chart is also displayed. Despite the SAR images had been acquired three days before the ice chart was published, the ice edges of the ice chart match well with the SAR mosaic in most parts because the same SAR data were used. In overall, the discriminations between ice and non-ice, old ice and other ice types, and detection of new ice patches look reasonable. However, some young ice patches, for example the ice patches between the Svalbard archipelago, are misclassified as the first-year ice. Figure 8 shows another daily mosaic made by the images acquired on the same day of the ice chart publication. Considering notable ice drift in the backscattering images in Figure 7 and 8, the SAR-based ice classification results in both figures look consistent, well in line with the ice drift. Although the weekly ice chart is supposed to represent the averaged ice status in the past few days, the actual ice distribution on the actual date of the publication can be largely different. This example shows a clear potential of near-real time service of ice type classification.

Figure 9 and 10 show the same mosaics for the case in the summer season. As shown in Table 6 and 7, the misclassifications for the mixed first-year ice into old ice are pronounced in the large ice patches north to Svalbard, while the ice edge positions of the ice chart and the classification result are in well agreement with each other.

To cope with the ambiguous classification for the winter season ice types with low accuracy, we conducted a test with the ~~further simplification of ice types by combining the new ice, young ice, and first-year ice into the “mixed” first-year ice, and then training new classifiers.~~three-class classification, and Table ~~5~~ 8 and ~~6~~ 9 show the resulting confusion matrices ~~for the three-class classifiers~~. The $\kappa$ for FC1, FC2, and FC3 were ~~0.84, 0.86, and 0.92~~0.83, 0.84, and 0.84 in ~~2018 data~~DS1, and ~~0.80, 0.80, and 0.53~~0.75, 0.75, and 0.74 in ~~2019 data~~DS2, respectively. The dramatic increase in the accuracy of the mixed first-year ice indicates that the misclassification for the new ice, young ice, and first-year ice was mostly among themselves. However, the accuracy decrease from ~~2018 data~~DS1 to ~~2019 data~~DS2 was at a similar level to the case of the five-class classification. This could have been caused by inconsistent labeling in the reference ice chart.

Figure ~~9~~ 11 shows an example of the inconsistent labeling in the reference ice chart. The SoDs from the NIC ice charts are superimposed on the Sentinel-1 backscattering images. The same ice floe (red outline) is classified differently in two different ice charts (old ice on the left panel and first-year ice on the right panel) although it looks almost the same in the corresponding SAR backscattering images. It should be noted that training with ice chart might have included mislabeled small features even if the image selection based on ice edge matching was successful. Furthermore, the boundaries between different ice types in the ice chart are normally not as precise as those in the SAR image-based classification results. Therefore, the lower classification accuracies compared to those in the previous studies (80% in Zakhvatkina et al., 2013; 91.7% in Liu et al., 2015; 87.2% in Aldenhoff et al., 2018), which used manually classified ice maps as training and validation reference, are expected. Unfortunately, we could not find an official report regarding the accuracy of the NIC ice chart information. It might be not enough to assess the quality of the classifier output when it is trained with, and evaluated against, only NIC ice charts. The accuracy could be indirectly investigated by comparing the output from our classifier against another data source, such as OSI

SAF sea ice type product (OSI-403-c). The ice classes of OSI-403-c are assigned from atmospherically corrected brightness temperatures of passive microwave radiometers (SSMIS and AMSR2) and backscatter values of radar scatterometer (ASCAT), using a Bayesian approach (Aaboe et al., 2018). Table 10 shows the confusion matrices for our three-class classifiers when their prediction results are compared with the OSI-403-c product as reference. Comparing with the results in Table 9, the accuracies for open water decreased from by 6%; however, this is mainly because the ice concentration threshold for ice-water discrimination in OSI-403-c is 35% which is higher than 20% that we set in our preprocessing of NIC ice chart (Section 2.2.1), thus areas with low ice concentration in marginal ice zone are most likely annotated as open water in OSI-403-c. For first-year ice, large portions (72%) are misclassified as old ice. This might be partly explained from the Figure 12, which shows the ice classes in NIC ice chart and OSI-403-c for the same publication date. A large extent of old ice in NIC ice chart is annotated as multi-year ice in OSI-403-c. As our classifiers were trained with NIC ice chart, it is natural to result in more old ice for the area where the ice type is classified as first-year ice in OSI-403-c. For old ice, the accuracy was the highest, 98%. Finding the reason for the clear discrepancy of the extent of first-year ice between the NIC ice chart and OSI-403-c is beyond the scope of this study, however, it should be noted that an elaborate future work for cross calibrating ice types in different ice charts are necessary.

~~Unfortunately, t~~The proposed algorithm has several limitations. First of all, the variations in radar backscattering and its corresponding image textures due to seasonal changes were not properly captured. Although day-of-the-year was tested as a seasonality variable in the FC3 feature configuration, the result did not show any improvement. This is because~~ day-of-the-year might not correspond to the same temperature, fluxes, and weather regimes~~ SAR image features, which partially reflect temperature fluxes and weather regimes, might not correspond to day-of-the-year. Second, the proposed method struggles when the same type of sea ice is located on different ~~marginal sides~~edges of the range swath of SAR images because the incidence angle dependence could not be normalized perfectly. An example of such a failure can be seen along the image boundaries at ~~80N, 35E~~79.5N, 45E in Figure 7 and ~~82.5N, 60E~~79N, 50E in Figure 8, approximately. Third, some artifacts were observed under ~~an extreme marine condition~~large ocean swells. In the classified results in the bottom right panel of Figure 8, there is a misclassified ~~FYI~~ first-year ice patch (yellow) in the open water area. According to the high resolution sea surface winds data from SAR on the Sentinel-1 satellites (https://data.nodc.noaa.gov/cgi-bin/iso?id=gov.noaa.nodc:SAR-WINDS-S1)~~NOAA SAR wind image service, ANSWRS 2.0~~, the wind speed ranged from 17 to 21 m/s at the time of image acquisition heavily roughing the water surface. Although we have included images with both high and low wind conditions in our training data, the image textures of wind roughened water surface and ice were confused in some cases, and the same happened in the image textures of calm water surface and smooth level ice.

## 4 Conclusion

A new semi-automated SAR-based sea ice type classification scheme was proposed in this study. For the first time several ice types ~~can be~~were successfully identified on Sentinel-1 SAR imagery in winter season, while only an ice-water discrimination was feasible in summer season. The main technological innovation is two-fold: i) minimized manual work in the preparation of training and validation reference data and ii) more objective evaluation of the SAR-based sea ice type classifier compared to the previous studies conducted with small number of images and customized ice type references from informal sources. A conventional approach for selecting training/testing data by anonymous human ice expert is undesirable not only because it is laborious, but also due to subjectivity and lack of standardization in the assessment of the automated classifier. Therefore, the performance from different literature sources cannot be intercompared directly.

Test results from the datasets of ~~two winter seasons~~winter season acquired over the Fram Strait and the Barents Sea area showed overall accuracies of ~~85% and 58%~~87% and 60% and the Cohen's kappa coefficients ~~$\kappa$~~ of ~~0.80 and 0.67~~0.75 and 0.67 for the three-class and five-class ice type classifiers, respectively. These are slightly lower than the numbers in the previous studies, and the errors are attributed not only to the automated algorithm but also to the inconsistency of the ice charts and the high level of their generalization. Test results from the datasets of summer seasons showed overall accuracy of 67% and the Cohen's kappa coefficient of 0.78 for the three-class classifiers. Considering the misclassifications in different ice types were among themselves, the three-class classifiers performed well at least as an ice-water discriminator with accuracy of 98%.

Based on the results, we envisage that three-class ice type classification from SAR imagery would be useful for making a global sea ice type product like ~~EUMETSAT OSI-403-C~~OSI SAF OSI-403-c with higher spatial resolution. The proposed approach importantly showed that a daily ice type mapping from the Sentinel-1 data is feasible and can help capture details of short-term changes in the stage of sea ice development. Based on the achieved results, we believe that the proposed approach may be efficiently used for operational ice charting services for supporting navigation in the Arctic.

## Code/Data availability

Not applicable

## Author contributions

JP and AK formulated the research plan, JP and AK developed the algorithm, JP implemented the algorithm and performed the data processing, JP, AK, MB, JW, MH, and HK carried out the analyses, and JP wrote the paper.

## Competing interests

The authors declare that they have no conflict of interests.


## Financial support

This work was supported by the French Service Hydrographique et Océanographique de la Marine (SHOM) under SHOM-ImpSIM Project 111222, the Research Council of Norway and the Russian Foundation for Basic Research under NORRUSS Project 243608, SONARC, and the Korea Polar Research Institute under grant number PE20080.

## References


Aaboe, S., Breivik, L.-A., and Eastwood, S.: Improvement of OSI SAF product of sea ice edge and sea ice type. EUMETSAT Meteorological Satellite Conference, Geneva (Switzerland), 22-26 September 2014.

Adnan, M. N., and Islam, M. Z., One-Vs-All Binarization Technique in the Context of Random Forest, Proc. European Symposium on Artificial Neural Networks, Computational Intelligence and Machine Learning, Bruges (Belgium), 22-24 April 2015.

Aldenhoff, W., Heuzé, C., and Eriksson, L.: Comparison of ice/water classification in Fram Strait from C- and L-band SAR imagery. Ann. Glaciol., 59(76pt2), 112-123. doi:10.1017/aog.2018.7, 2018.

Anand, R., Mehrotra, K., Mohan, C. K., and Ranka, S.: Efficient classification for multiclass problems using modular neural networks, IEEE T. Neural Networ., 6(1), 117-124, doi:10.1109/72.363444, 1995.

Barber, D. G. and LeDrew, E. F.: SAR sea ice discrimination using texture statistics: A multivariate approach. Photogramm. E. Rem. S., 57(4), 385-395, 1991.

Cohen, J.: A coefficient of agreement for nominal scales, Educ. Psychol. Meas., 20(1), 37–46, doi:10.1177/001316446002000104, 1960.

Cortes, C. and Vapnik, V.: Support-vector networks, Mach. Learn., 20(3), 273-297, doi: 10.1007/BF00994018, 1995.

Deng, H. and Clausi, D. A.: Unsupervised segmentation of synthetic aperture radar sea ice imagery using a novel Markov random field model," IEEE T. Geosci. Remote, 43(3), 528-538, doi:10.1109/TGRS.2004.839589, 2005.

Dierking, W.: Mapping of different sea ice regimes using images from Sentinel-1 and ALOS synthetic aperture radar, IEEE T. Geosci. Remote, 48(3), 1045-1058, doi:10.1109/TGRS.2009.2031806, 2010.

ESRI (Environmental Systems Research Institute, Inc.): ESRI Shapefile Technical Description, An ESRI White Paper, 1998. Available at: http://downloads.esri.com/support/whitepapers/mo_/shapefile.pdf

Fernández-Delgado, M., Cernadas, E., Barro, S., and Amorim, D.: Do we need hundreds of classifiers to solve real world classification problems?, J. Mach. Learn. Res., 15, 3133-3181, 2014.

GDAL/OGR contributors: GDAL/OGR Geospatial Data Abstraction software Library, Open Source Geospatial Foundation, 2019. URL https://gdal.org

Gill, J. P.S., Yackel, J. J., Geldsetzer, T., and Fuller, M. C.: Sensitivity of C-band synthetic aperture radar polarimetric parameters to snow thickness over landfast smooth first-year sea ice, Remote Sens. Environ., 166, 34-49, doi:10.1016/j.rse.2015.06.005, 2015.

Haralick, R. M., Shanmugam, K., Dinstein, I.: Textural features for image classification, IEEE T. SYST. MAN. CY.-S., SMC-3(6), 610-621, doi:10.1109/TSMC.1973.4309314, 1973.

Hersbach, H., Stoffelen, A., and de Haan, S.: An improved C-band scatterometer ocean geophysical model function: CMOD5, J. Geophys. Res., 112, C03006, doi:10.1029/2006JC003743, 2007.

Heinrichs, J. F., Cavalieri, D. J., and Markus, T.: Assessment of the AMSR-E sea ice concentration product at the ice edge using RADARSAT-1 and MODIS imagery, IEEE T. Geosci. Remote, 44(11), 3070-3080, doi: 10.1109/TGRS.2006.880622, 2006.

Ho, T. K.: The random subspace method for constructing decision forests, IEEE T. Pattern Anal., 20(8), 832-844, doi:10.1109/34.7096011998, 1998.

Isleifson, D., Galley, R. J., Barber, D. G., Landy, J. C., Komarov, A. S., and Shafai, L.: A study on the C-band polarimetric scattering and physical characteristics of frost flowers on experimental sea ice," IEEE T. Geosci. Remote, 52(3), 1787-1798, doi:10.1109/TGRS.2013.2255060, 2014.

JCOMM (Joint WMO-IOC Technical Commission for Oceanography and Marine Meteorology): Ice chart colour code standard, JCOMM Technical Report No. 24, Tech. rep., World Meteorological Organization, Geneva, Switzerland, 2014a.

JCOMM (Joint WMO-IOC Technical Commission for Oceanography and Marine Meteorology): SIGRID-3: a vector archive format for sea ice georeferenced information and data, JCOMM Technical Report No. 23, Tech. rep., World Meteorological Organization, Geneva, Switzerland, 2014b.

Johannessen, O.M., Alexandrov, V., Frolov, I.Y., Sandven, S., Pettersson, L.H., Bobylev, L.P., Kloster, K., Smirnov, V.G., Mironov, Y.U., and Babich, N.G.: Remote sensing of sea ice in the Northern Sea route: Studies and applications, Springer, Berlin, Heidelberg, doi:10.1007/978-3-540-48840-8, 2006.

Karvonen, J.: A sea ice concentration estimation algorithm utilizing radiometer and SAR data. The Cryosphere, 8, 1639-1650, doi:10.5194/tc-8-1639-2014, 2014.

Karvonen, J., Vainio, J., Marnela, M., Eriksson, P., and Niskanen, T.: A comparison between high-resolution EO-based and ice analyst-assigned sea ice concentrations, IEEE J. Sel. Top. Appl., 8(4), 1799-1807, 2015.

Karvonen, J.: Baltic sea ice concentration estimation using Sentinel-1 SAR and AMSR2 microwave radiometer data, IEEE T. Geosci. Remote, 55(5), 2871-2883, doi:10.1109/TGRS.2017.2655567, 2017.

Keller, M. R., Gifford, C. M., Walton, W. C., and Winstead, N. S.: Ice analysis based on active and passive radar images, U.S. Patent 9652674 B2, May 16, 2017. Available at: https://patents.google.com/patent/US9652674

Kohavi, R.: A Study of cross-validation and bootstrap for accuracy estimation and model selection, Proceedings of the 14th international joint conference on Artificial intelligence, Montreal, Canada, 20-25 August,1995, 2, 1137-1143, 1995.

Leigh, S., Wang, Z., and Clausi, D. A.: Automated ice-water classification using dual polarization SAR satellite imagery, IEEE T. Geosci. Remote, 52(9), 5529–5539, doi:10.1109/TGRS.2013.2290231, 2014.

Liu, H., Guo, H., and Zhang, L.: SVM-based sea ice classification using textural features and concentration from RADARSAT-2 dual-pol ScanSAR data, IEEE J. Sel. Top. Appl., 8(4), 1601–1613, doi:10.1109/JSTARS.2014.2365215, 2015.

Louppe, G.: Understanding random forests: From theory to practice, PhD Thesis, U. of Liege, 2014.

Mahmud, M. S., Geldsetzer, T., Howell, S. E. L., Yackel, J. J., Nandan, V., and Scharien, R. K.: Incidence angle dependence of HH-polarized C- and L-band wintertime backscatter over Arctic sea ice, IEEE T. Geosci. Remote, 56(11), 6686-6698, doi: 10.1109/TGRS.2018.2841343, 2018.

Mäkynen, M. and Karvonen, J.: Incidence angle dependence of first-year sea ice backscattering coefficient in Sentinel-1 SAR imagery over the Kara Sea, IEEE T. Geosci. Remote, 55(11), 6170-6181, doi:10.1109/TGRS.2017.2721981, 2017.

Mäkynen, M. P., Manninen, A. T., Simila, M. H., Karvonen, J. A., and Hallikainen, M. T.: Incidence angle dependence of the statistical properties of C-band HH-polarization backscattering signatures of the Baltic Sea ice, IEEE T. Geosci. Remote, 40(12), 2593-2605, doi:10.1109/TGRS.2002.806991, 2002.

Miranda, N.: S-1 constellation product performance status, SeaSAR 2018, Frascati, Italy, 7-10 May 2018. Available at: http://seasar2018.esa.int/files/presentation216.pdf

Aaboe, S., Breivik, L.-A., Sørensen, A., Eastwood, S., and Lavergne, T.: Global sea ice edge and type product user's manual OSI-402-c & OSI-403-c, Ocean & Sea Ice Satellite Application Facilities (OSI SAF), version 2.3, 2018. Available at: http://osisaf.met.no/docs/osisaf_cdop3_ss2_pum_sea-ice-edge-type_v2p3.pdf

Park, J.-W., Korosov, A. A., Babiker, M., Sandven, S., and Won, J.-S.: Efficient thermal noise removal for Sentinel-1 TOPSAR cross-polarization channel, IEEE T. Geosci. Remote, 56(3), 1555–1565, doi:10.1109/TGRS.2017.2765248, 2018.

Park, J.-W., Won, J.-S., Korosov, A. A., Babiker, M., and Miranda, N.: Textural noise correction for Sentinel-1 TOPSAR cross-polarization channel images, IEEE T. Geosci. Remote, 57(6), 4040-4049, doi:10.1109/TGRS.2018.2889381, 2019.

Partington, K., Flynn, T., Lamb, D., Bertoia, C., and Dedrick, K: Late twentieth century Northern Hemisphere sea-ice record from the U.S. National Ice Center ice charts, J. Geophys. Res., 108(C11), doi:10.1029/2002JC001623, 2003.

Pastusiak, T.: Accuracy of sea ice data from remote sensing methods, its impact on safe speed determination and planning of voyage in ice-covered areas, International Journal on Marine Navigation and Safety of Sea Transportation, 10(2), 229-248, doi:10.12716/1001.10.02.06, 2016.

Pedregosa, F., Varoquaux, G., Gramfort, A., Michel, V., Thirion, B., Grisel, O., Blondel, M., Prettenhofer, P., Weiss, R., Dubourg, V., Vanderplas, J., Passos, A., Cournapeau, D., Brucher, M., Perrot, M., and Duchesnay, E.: Scikit-learn: Machine learning in Python, J. Mach. Learn. Res., 12, 2825-2830, doi:10.1016/j.patcog.2011.04.006, 2011.

Ressel, R., Frost, A., and Lehner, S.: A neural network-based classification for sea ice types on X-band SAR images, IEEE J. Sel. Top. Appl., 8(7), 3672-3680, doi:10.1109/JSTARS.2015.2436993, 2015.

Richards, F. J.: A flexible growth function for empirical use, J. Exp. Bot., 10(29), 290-300, doi: 10.1093/jxb/10.2.290, 1959.

Scharien, R. K., Landy, J., and Barber, D. G.: First-year sea ice melt pond fraction estimation from dual-polarisation C-band SAR – Part 1: In situ observations, The Cryosphere, 8, 2147-2162, doi:10.5194/tc-8-2147-2014, 2014

Scheuchl, B., Flett, D., Caves, R., and Cumming, I.: Potential of RADARSAT-2 data for operational sea ice monitoring, Can. J. Remote Sens., 30(3), 448-471, 2004.

Shokr, M. E.: Evaluation of second-order texture parameters for sea ice classification from radar images, J. Geophys. Res.-Oceans, 96(C6), 10625-10640, 1991.

Smedsrud, L. H., Halvorsen, M. H., Stroeve, J. C., Zhang, R., and Kloster, K.: Fram Strait sea ice export variability and September Arctic sea ice extent over the last 80 years, The Cryosphere, 11, 65-79, doi:10.5194/tc-11-65-2017, 2017.

Soh, L.-K. and Tsatsoulis, C.: Texture analysis of SAR sea ice imagery using gray level co-occurrence matrices, IEEE T. Geosci. Remote, 37(2), 780-795, doi:10.1109/36.752194, 1999.

Wang, L., Scott, K. A., and Clausi, D. A., Sea ice concentration estimation during freeze-up from SAR imagery using a convolutional neural network, Remote Sens-Basel, 9(5), doi:10.3390/rs9050408, 2017.

Zakhvatkina, N. Y., Alexandrov, V. Y., Johannessen, O. M., Sandven, S., and Frolov, I. Y.: Classification of sea ice types in ENVISAT synthetic aperture radar images, IEEE T. Geosci. Remote, 51(5), 2587-2600, doi:10.1109/TGRS.2012.2212445, 2013.

Zakhvatkina, N., Korosov, A., Muckenhuber, S., Sandven, S., and Babiker, M.: Operational algorithm for ice-water classification on dual-polarized RADARSAT-2 images, The Cryosphere, 11, 33-46, doi:10.5194/tc-11-33-2017, 2017.

Zakhvatkina, N., Smirnov, V., and Bychkova, I.: Satellite SAR data-based sea ice classification: An overview, Geosci. J., 9(4), 152, doi: 10.3390/geosciences9040152, 2019.

**Figures**

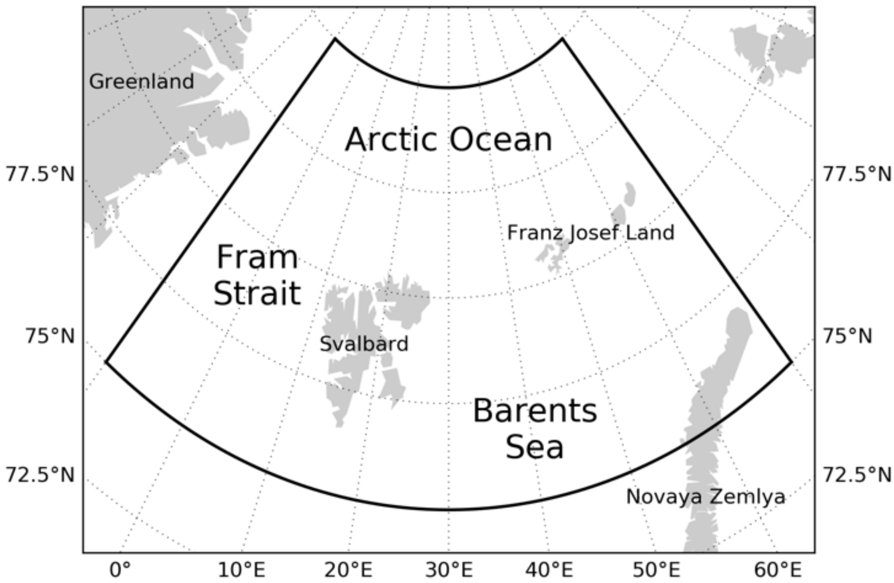


**Figure 1: Study area.**

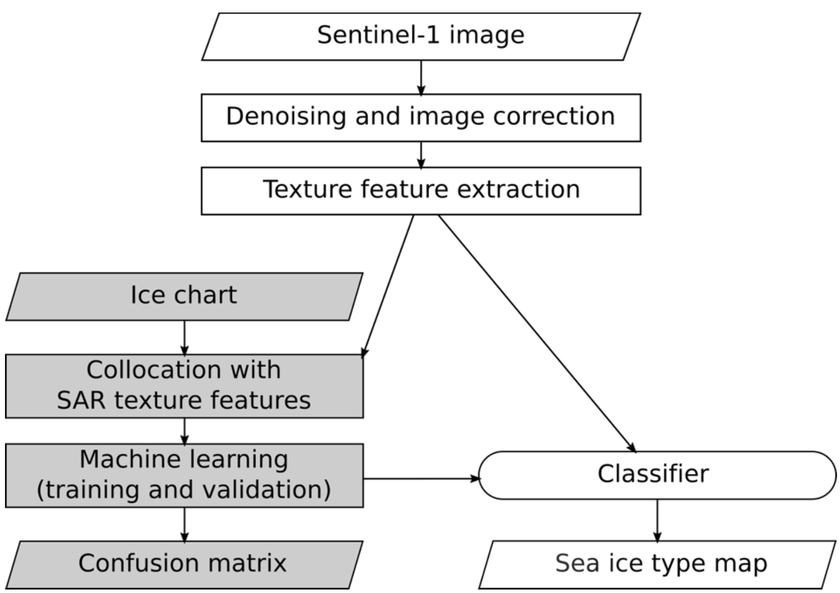


**Figure 2: Processing flowchart of the proposed algorithm. The gray color shows the training phase.**

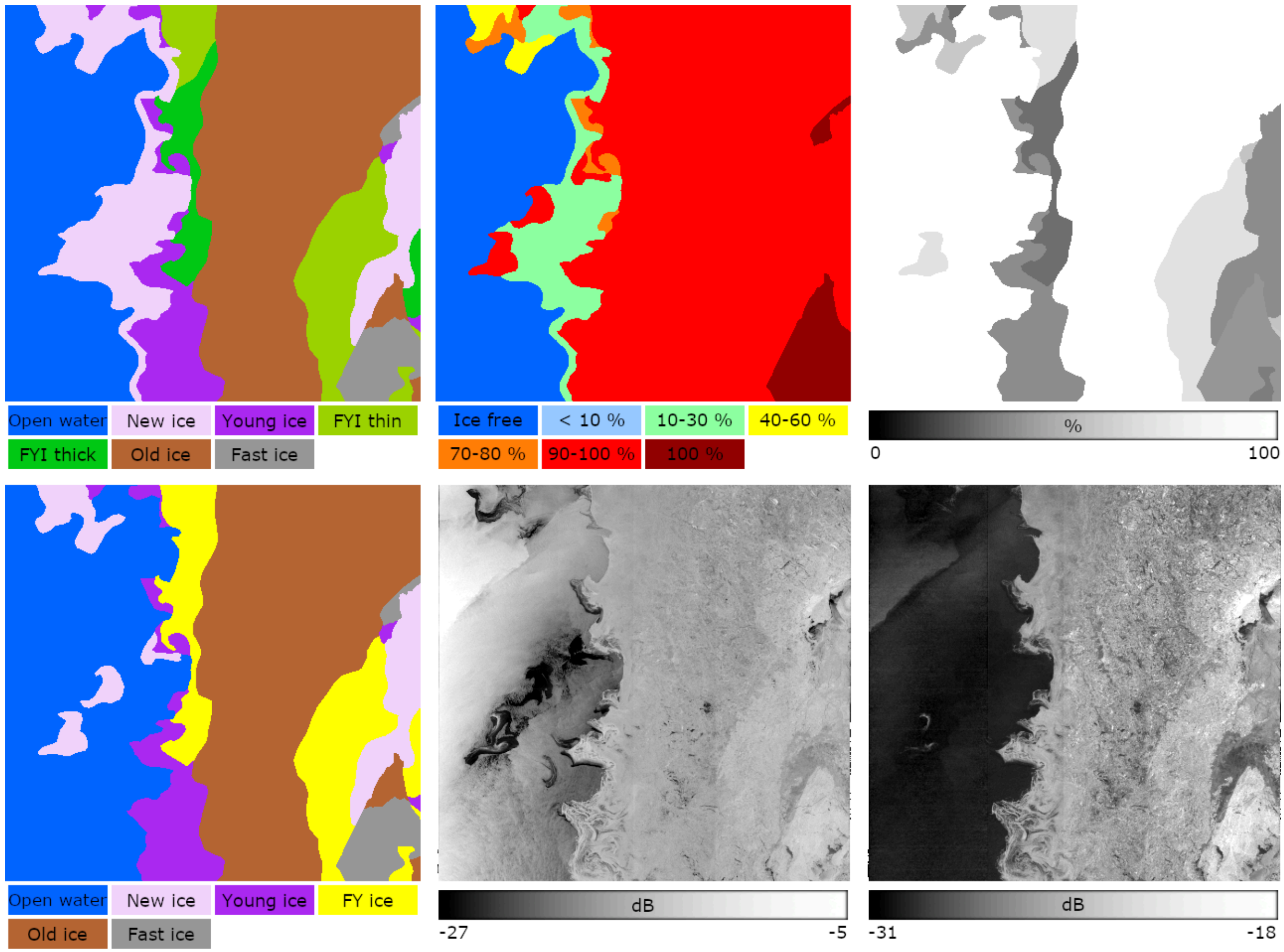


~~Figure 3: An example of the ice chart preprocessing. From the ice chart, stage of development (SoD; Top left), ice concentration (CT; Top center), and partial concentration of the dominant ice type (CP; Top right) maps are extracted. Then, some of the different SoDs are merged (e.g., thin and thick first-year ices are merged into a single label as first-year ice) and the area with low ice concentration is labeled as open water. The processed map of SoD (Bottom left) is related with textural features extracted from HH and HV polarization images (Bottom center and bottom right). Note that the NIC ice chart which was published on January 25, 2018, and the Sentinel-1 product S1B_EW_GRDM_1SDH_20180122T075237_20180122T075337_009281_010A4D_65AA acquired over the Fram Strait were used in this example.~~

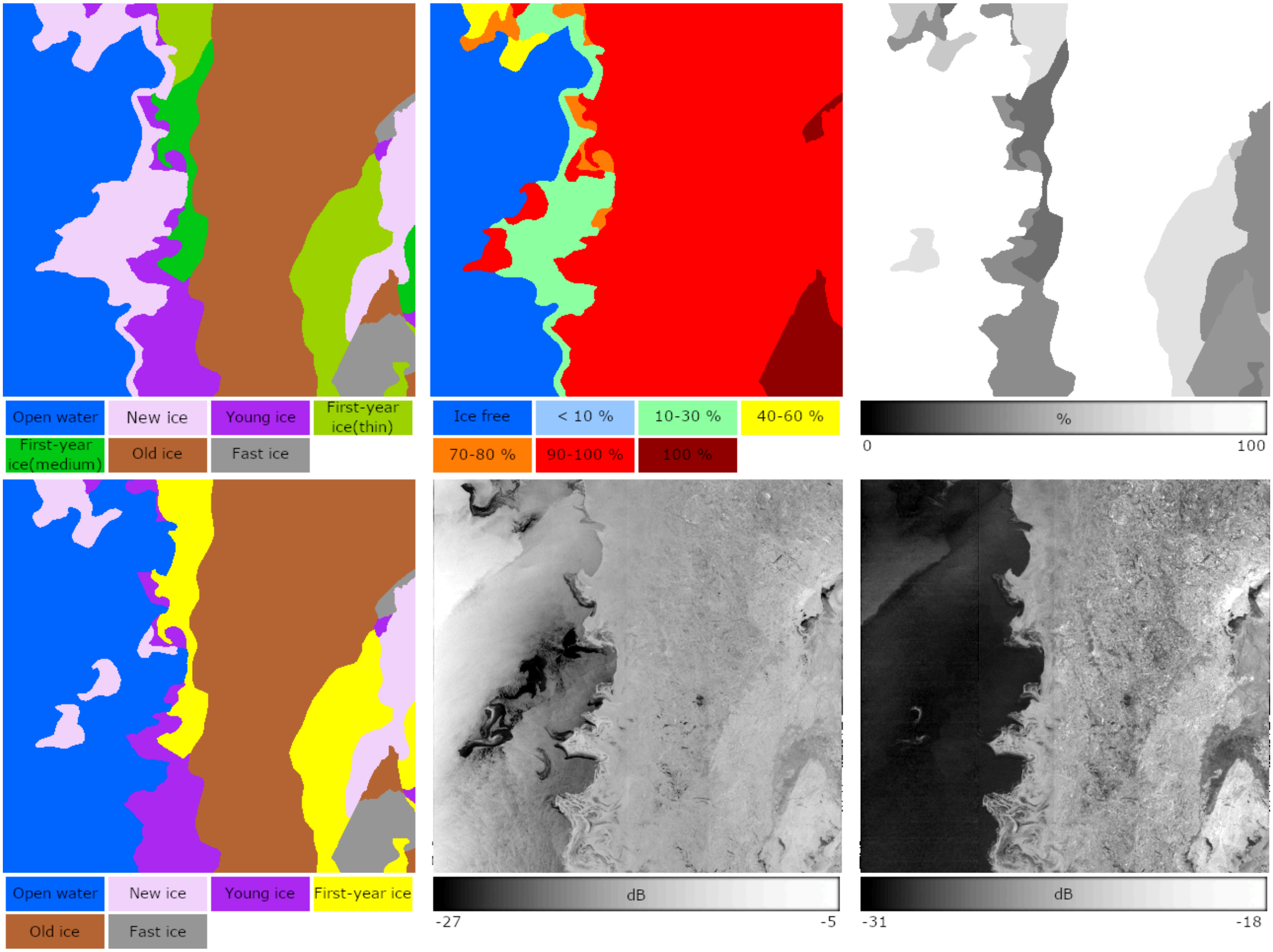


Figure 3: An example of the ice chart preprocessing. From the ice chart, stage of development (SoD; Top left), ice concentration (CT; Top center), and partial concentration of the dominant ice type (CP; Top right) maps are extracted. Then, some of the different SoDs are merged (e.g., thin and thick first-year ice are merged into a single label as first-year ice) and the area with low ice concentration is labeled as open water. The processed map of SoD (Bottom left) is related with textural features extracted from HH and HV polarization images (Bottom center and bottom right). Note that the NIC ice chart which was published on January 25, 2018, and the Sentinel-1 product S1B_EW_GRDM_1SDH_20180122T075237_20180122T075337_009281_010A4D_65AA acquired over the Fram Strait were used in this example.

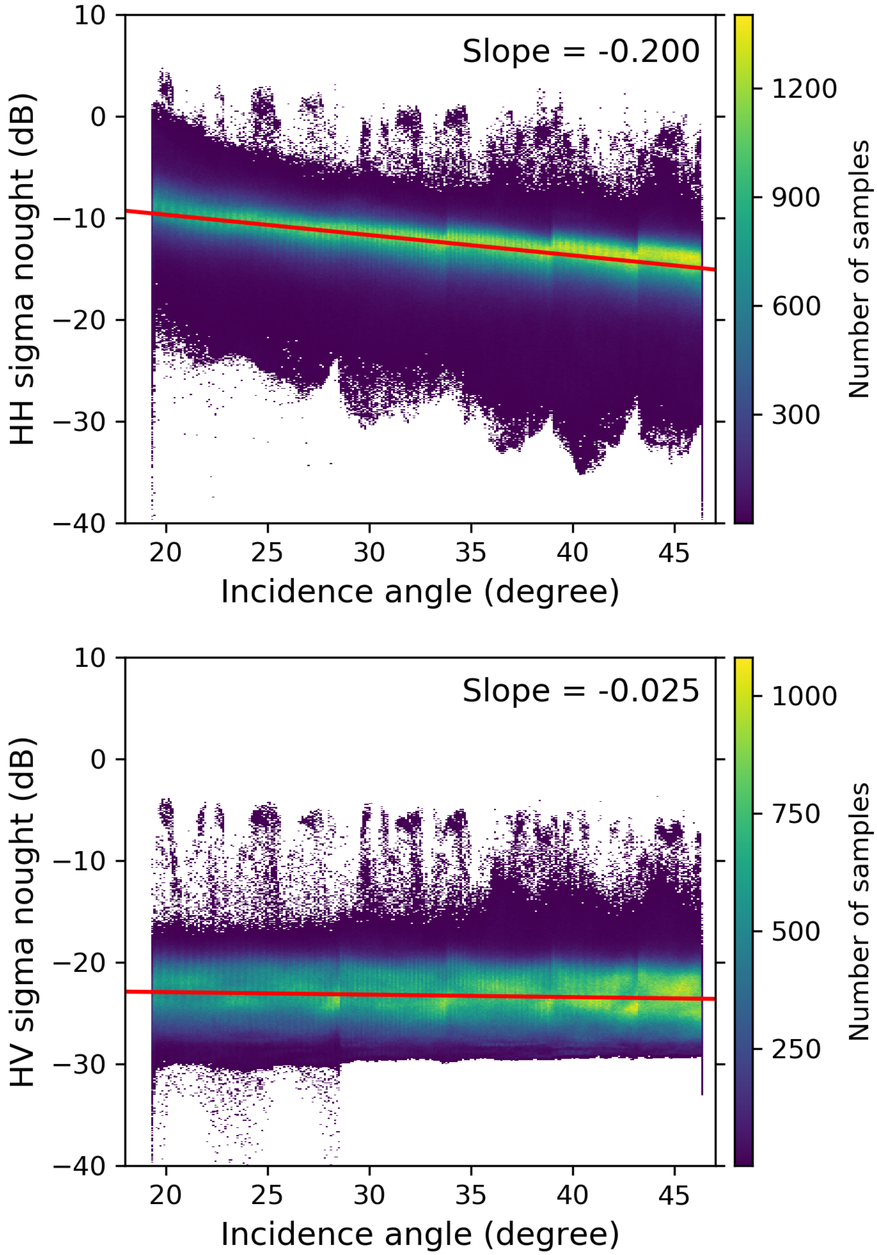


~~Figure 4: Two-dimensional histograms of incidence angle versus sigma nought for HH (top) and HV (bottom) polarization channels. Pixels covering various types of sea ice were merged so that the averaged property can be estimated. The best fit linear trends are shown with red lines.~~

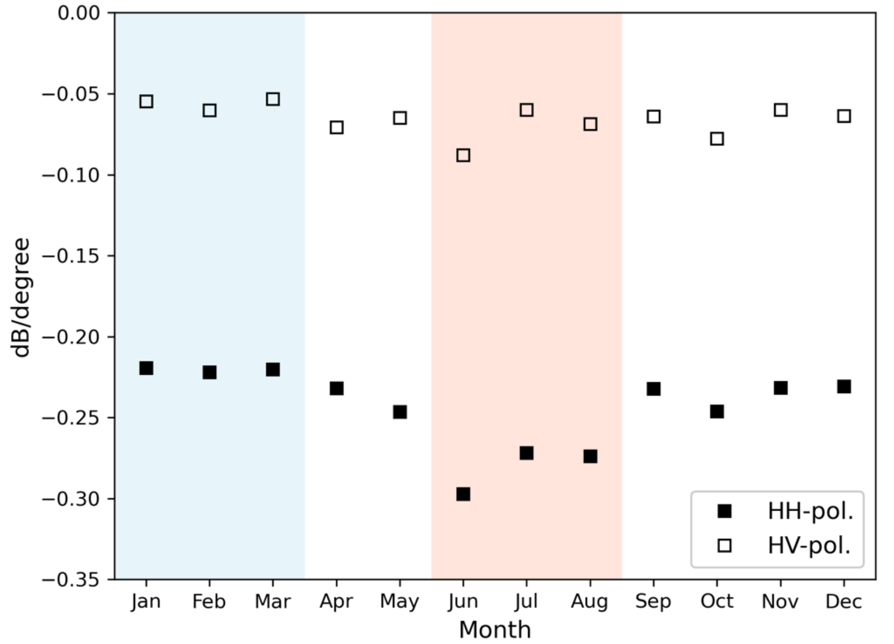


**Figure 4: Incidence angle dependences of sigma naught in HH (closed squares) and HV (open squares) polarization channels. Pixels covering various types of sea ice were merged so that the averaged property can be estimated. The blue and red zones indicate winter and summer seasons, respectively.**

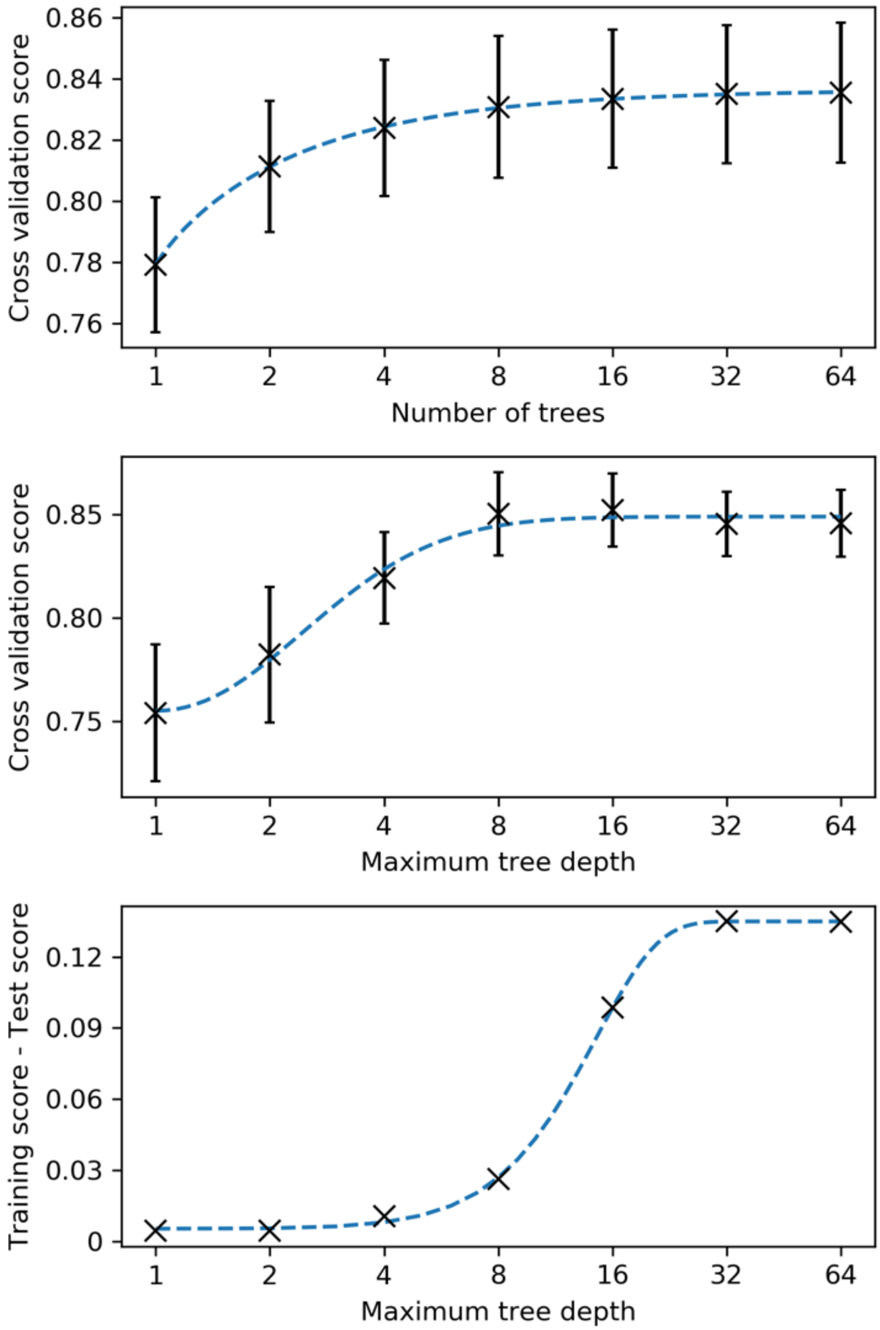


**Figure 5: Hyperparameter optimization using grid search results (cross). Dashed lines represent the best-fit Richards' Curve. (Top panel) The optimal values are extracted from the locations where the score increments per unit of each hyperparameter become lower than a threshold (e.g., 0.001). (Center panel) If the curve does not fit the grid search results well, (Bottom panel) the difference between training and test scores is used to find the locations where it does not exceed a threshold (e.g., 0.03) in order to avoid overfitting.**

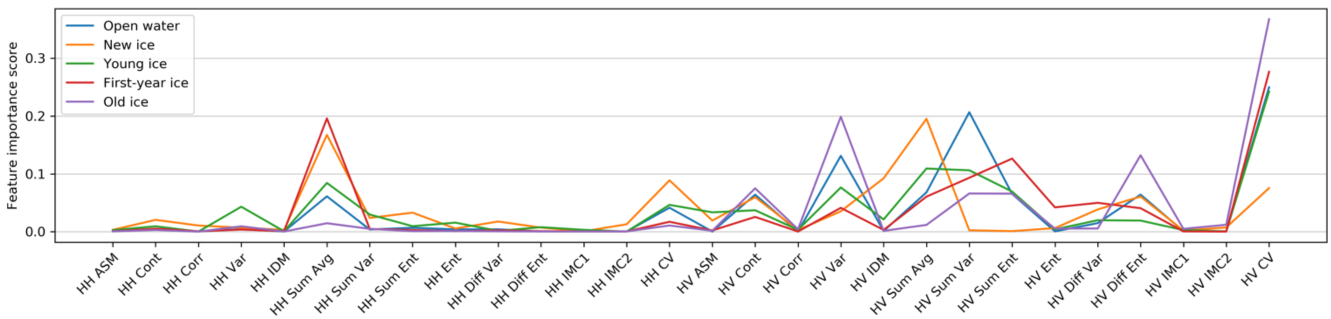


~~**Figure 6: Feature importances of the binary sub-classifiers. ASM: angular second moment; Cont: contrast; Corr: correlation; Var: variance; IDM: inverse difference moment; Sum Avg: sum average; Sum Var: sum variance; Sum Ent: sum entropy; Ent: entropy; Diff Var: difference variance; Diff Ent: difference entropy; IMC: information measures of correlation; CV: coefficient of variation. For definitions of each parameters, please refer to Haralick et al., 1973.**~~

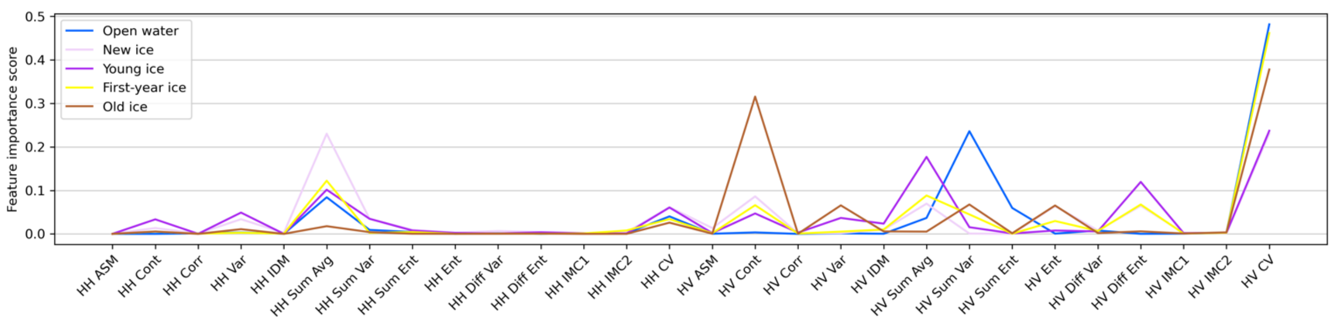


**Figure 6: Feature importances of the binary sub-classifiers. ASM: angular second moment; Cont: contrast; Corr: correlation; Var: variance; IDM: inverse difference moment; Sum Avg: sum average; Sum Var: sum variance; Sum Ent: sum entropy; Ent: entropy; Diff Var: difference variance; Diff Ent: difference entropy; IMC: information measures of correlation; CV: coefficient of variation. For definitions of each parameters, please refer to Haralick et al., 1973.**

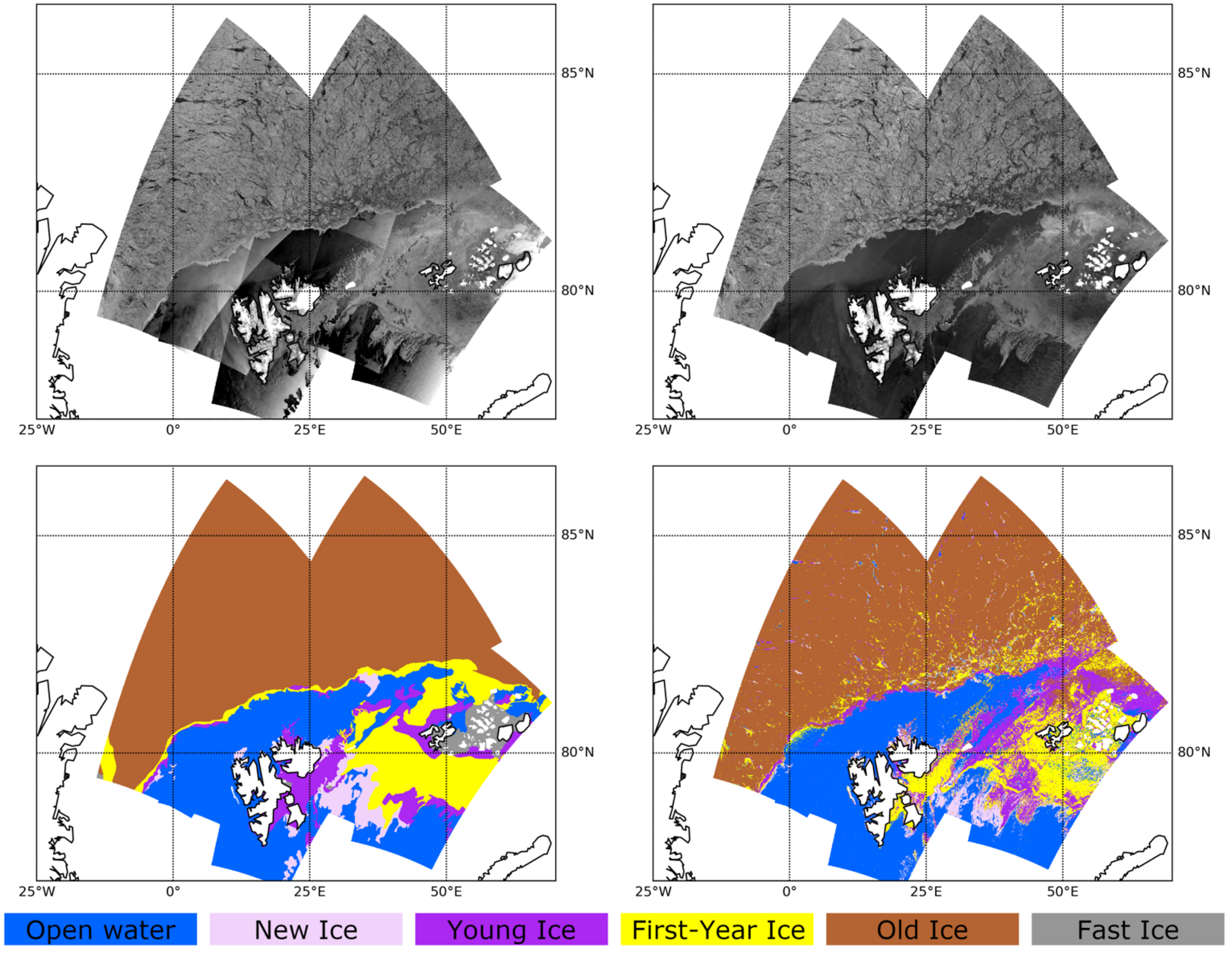


~~Figure 7: One-day mosaics of Sentinel-1A/1B images (Top left: HH, Top right: HV) and the ice classification result (Bottom right) on 5 February 2019. The publication date of the reference weekly ice chart is 8 February 2019 (Bottom left).~~

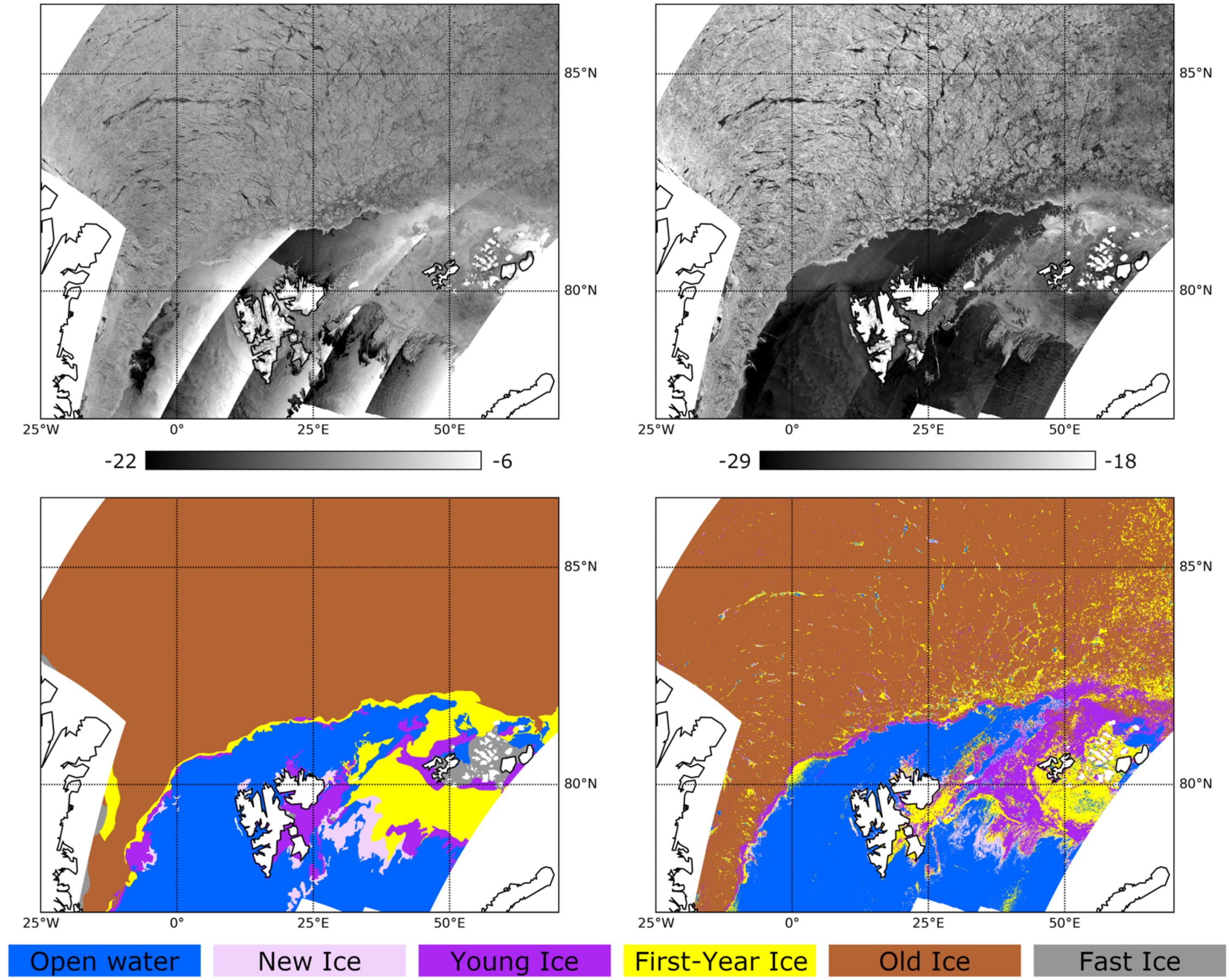


**Figure 7: One-day mosaics of Sentinel-1A/1B images (Top left: HH, Top right: HV) and the ice classification result (Bottom right) on 5 February 2019. The publication date of the reference weekly ice chart is 8 February 2019 (Bottom left).**

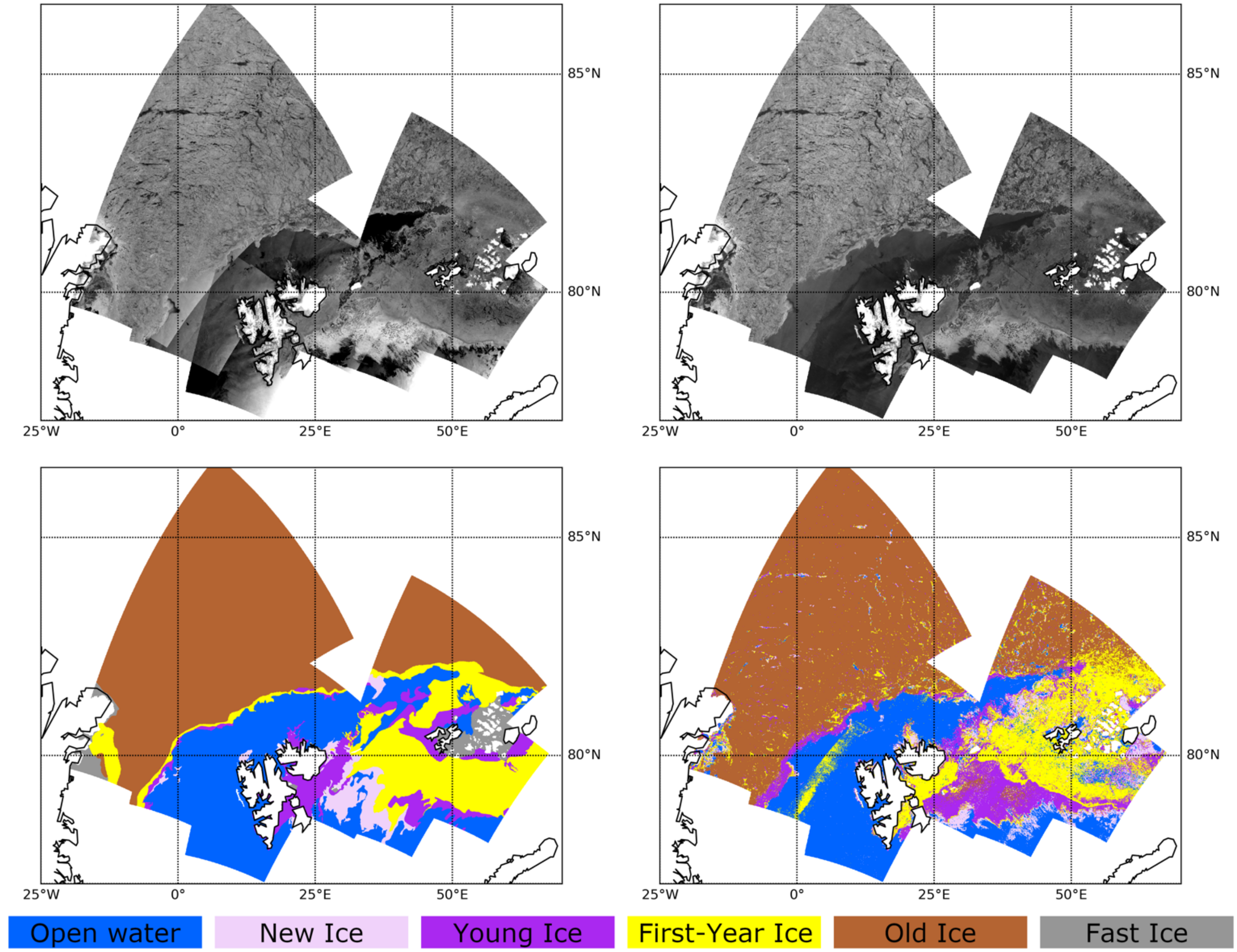


~~**Figure 8: One-day mosaics of Sentinel-1A/1B images (Top left: HH, Top right: HV) and the ice classification result (Bottom right) on 8 February 2019. The publication date of the reference weekly ice chart is 8 February 2019 (Bottom left).**~~

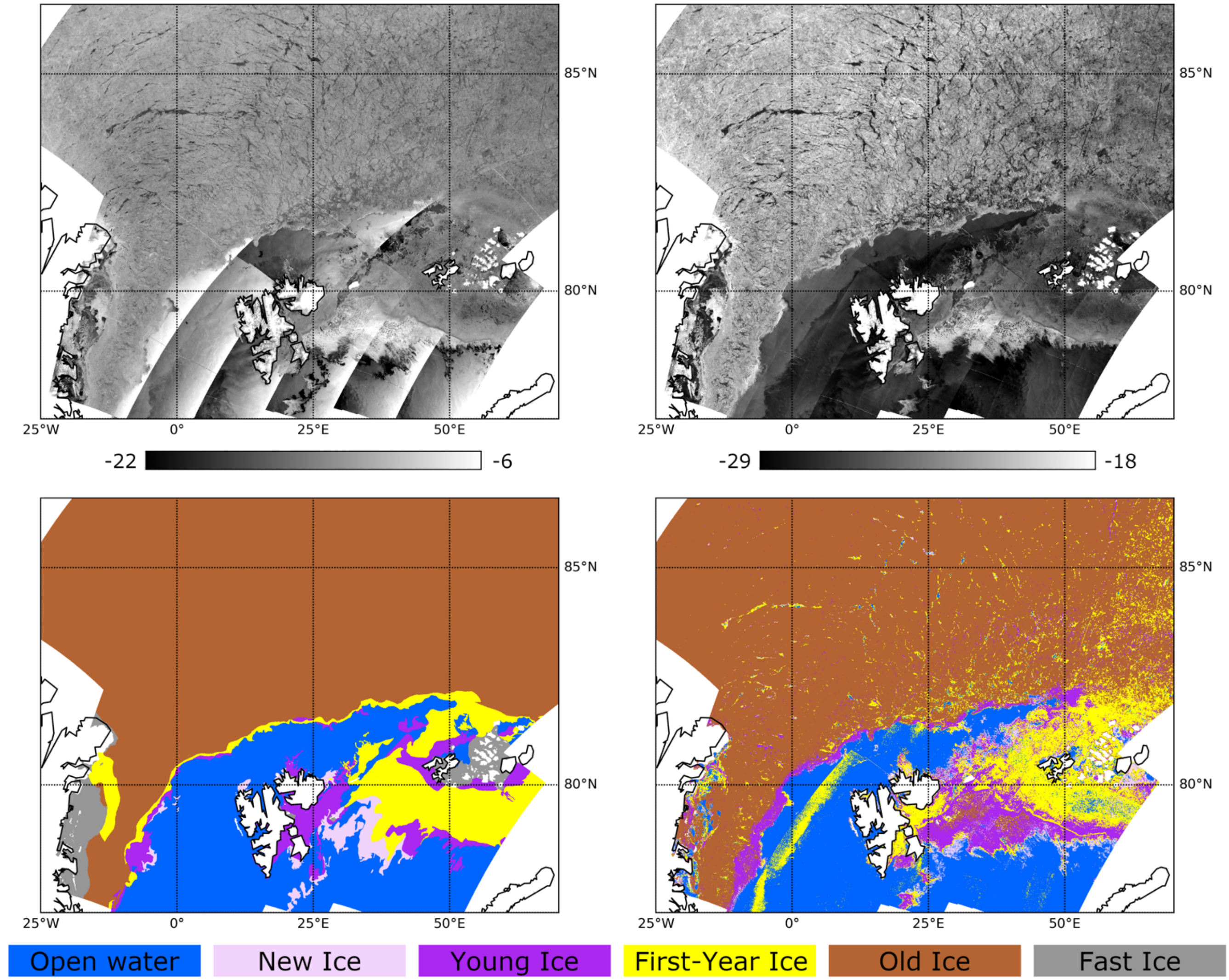


Figure 8: One-day mosaics of Sentinel-1A/1B images (Top left: HH, Top right: HV) and the ice classification result (Bottom right) on 8 February 2019. The publication date of the reference weekly ice chart is 8 February 2019 (Bottom left).

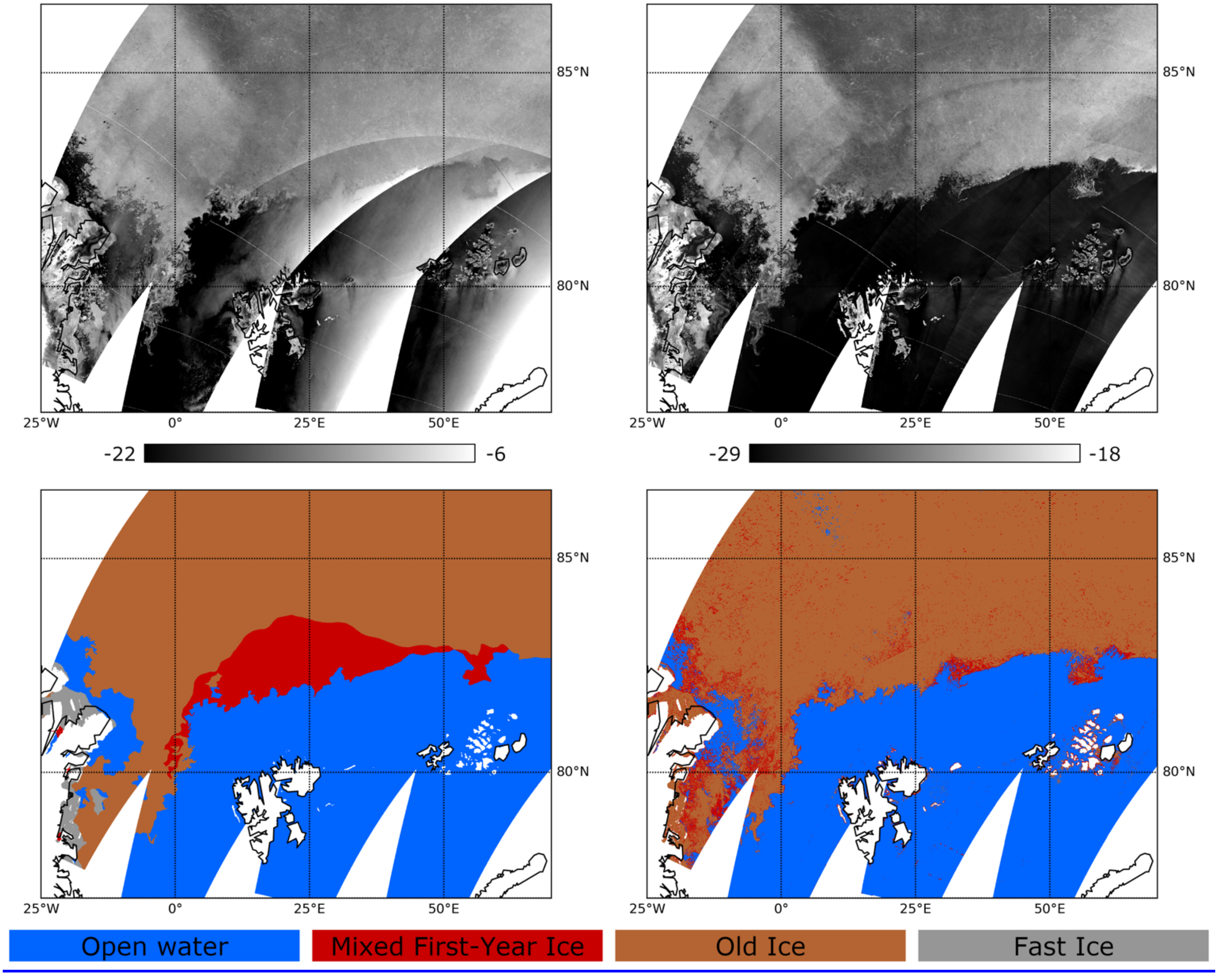


Figure 9: One-day mosaics of Sentinel-1A/1B images (Top left: HH, Top right: HV) and the ice classification result (Bottom right) on 13 August 2018. The publication date of the reference weekly ice chart is 16 August 2018 (Bottom left).

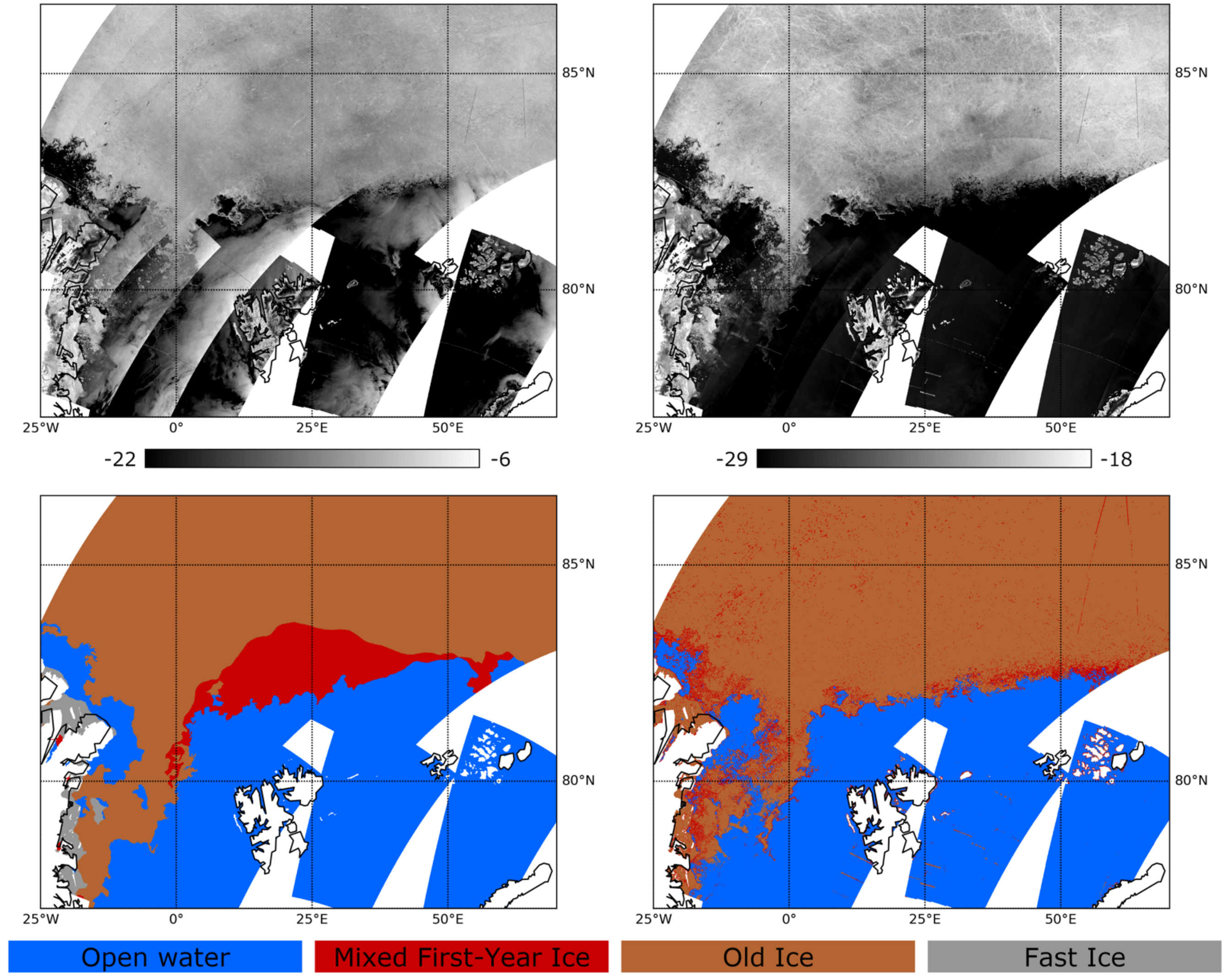


**Figure 10: One-day mosaics of Sentinel-1A/1B images (Top left: HH, Top right: HV) and the ice classification result (Bottom right) on 16 August 2018. The publication date of the reference weekly ice chart is 16 August 2018 (Bottom left).**

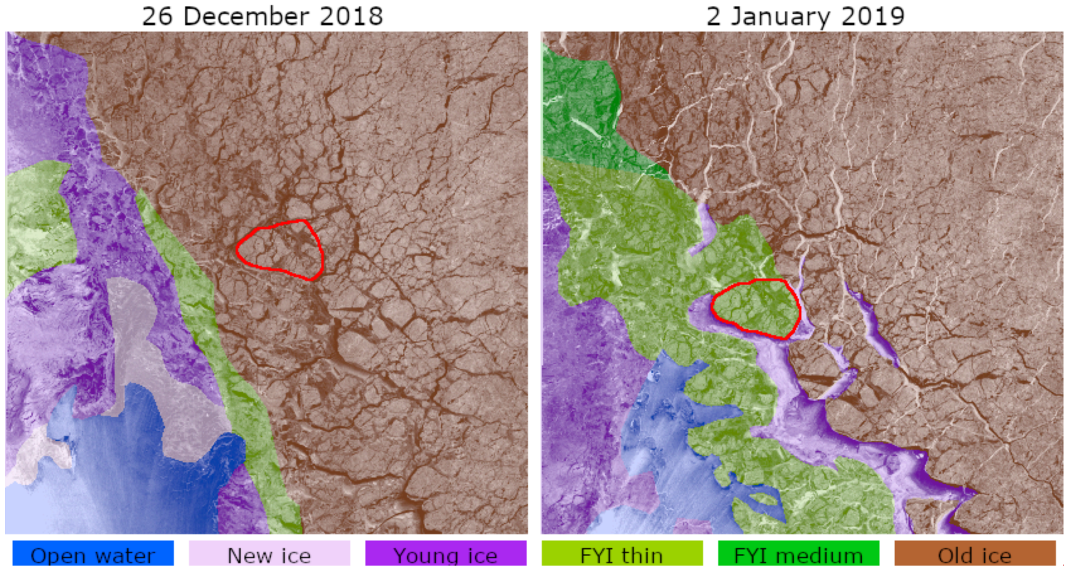


~~Figure 9: An example of the inconsistency of the ice charts. The SoDs from the NIC ice charts on different dates (26 December 2018 and 2 January 2019) are superimposed on the Sentinel-1 backscattering image of the corresponding dates. The same ice floe (red outline) is classified differently in each ice chart (old ice on the left panel and first-year ice on the right panel) despite of the similarity in the SAR backscattering images.~~

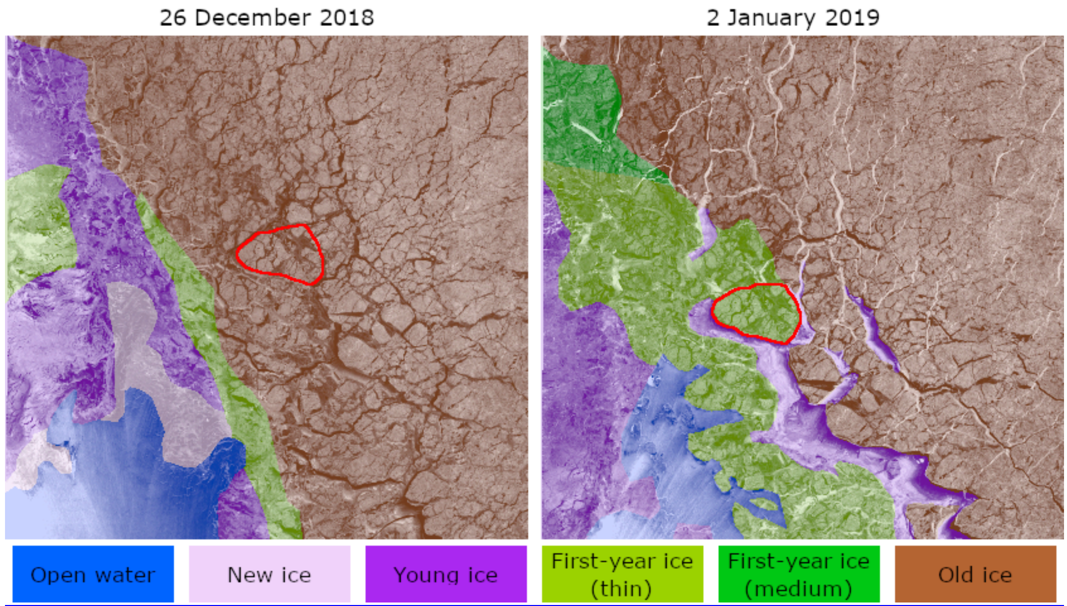


Figure 11: An example of the inconsistency of the ice charts. Note that the SoD labels and colors are of original NIC ice chart, while those in Figure 7 and 8 are of simplified version as described in Section 2.2.1.The SoDs from the NIC ice charts on different dates (26 December 2018 and 2 January 2019) are superimposed on the Sentinel-1 backscattering image of the corresponding dates. The same ice floe (red outline) is classified differently in each ice chart (old ice on the left panel and first-year ice on the right panel) despite of the similarity in the SAR backscattering images.

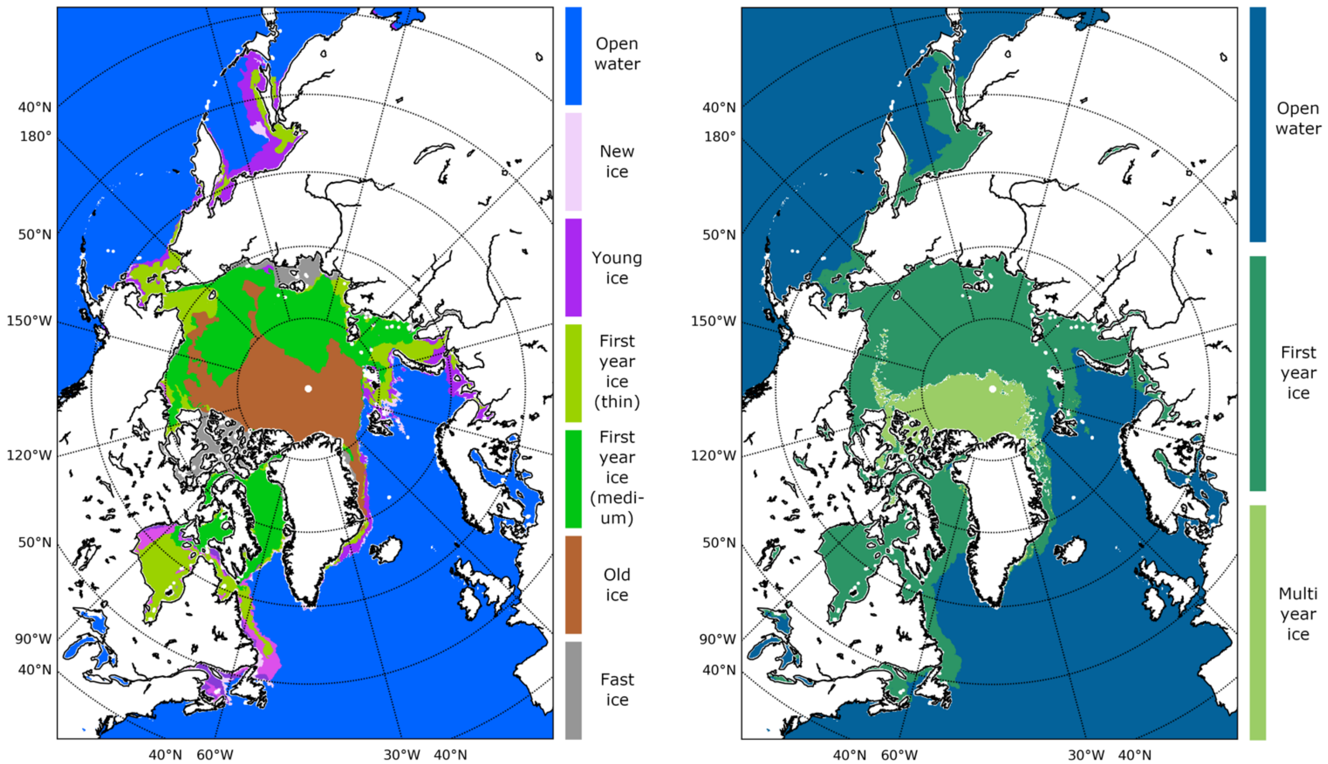


**Figure 12: The ice types in NIC ice chart (left) and OSI SAF sea ice type product (right) for the same date (8 Jan. 2019). Note that the SoD labels and colors follows those defined in each ice chart format.**

## Tables

**Table 1: Hyperparameters used for grid search**

| Parameters | Values | | | | | | |
|---|---|---|---|---|---|---|---|
| $N_T$ | 1 | 2 | 4 | 8 | 16 | 32 | 64 |
| $D$ | 1 | 2 | 4 | 8 | 16 | 32 | 64 |
| $N_F$ | 1 | 2 | 4 | 8 | 16 | 28 | |

**Table 2: Distribution of the image acquisition dates prior to the publication of the reference ice chart**

| | Training and test dataset (DS1) | | | | Validation dataset (DS2) | | | |
|---|---|---|---|---|---|---|---|---|
| Days prior to the date of ice chart publication | 3 | 2 | 1 | 0 | 3 | 2 | 1 | 0 |
| Winter | 124 | 168 | 77 | 50 | 78 | 75 | 67 | 61 |
| Summer | 119 | 125 | 112 | 65 | 87 | 67 | 48 | 30 |

**~~Table 2: Confusion matrix of the five-class RF classifier which was trained with and applied to the 2018 dataset~~**

| | | ~~Predicted~~ | | | | | | | | | | | | | | |
|---|---|---|---|---|---|---|---|---|---|---|---|---|---|---|---|---|
| | | ~~OW (open water)~~ | | | ~~NI (new ice)~~ | | | ~~YI (young ice)~~ | | | ~~FYI (first-year ice)~~ | | | ~~OI (old ice)~~ | | |
| | ~~case~~ | ~~FC1~~ | ~~FC2~~ | ~~FC3~~ | ~~FC1~~ | ~~FC2~~ | ~~FC3~~ | ~~FC1~~ | ~~FC2~~ | ~~FC3~~ | ~~FC1~~ | ~~FC2~~ | ~~FC3~~ | ~~FC1~~ | ~~FC2~~ | ~~FC3~~ |
| ~~Actual~~ | ~~OW~~ | **~~94.5~~** | **~~95.2~~** | **~~96.7~~** | ~~1.4~~ | ~~1.1~~ | ~~0.6~~ | ~~0.3~~ | ~~0.3~~ | ~~0.3~~ | ~~3.7~~ | ~~3.4~~ | ~~2.4~~ | ~~0.0~~ | ~~0.0~~ | ~~0.0~~ |
| | ~~NI~~ | ~~19.3~~ | ~~17.3~~ | ~~14.8~~ | **~~33.1~~** | **~~38.9~~** | **~~68.7~~** | ~~33.3~~ | ~~31.1~~ | ~~9.3~~ | ~~12.1~~ | ~~10.6~~ | ~~5.5~~ | ~~2.2~~ | ~~2.1~~ | ~~1.7~~ |
| | ~~YI~~ | ~~1.9~~ | ~~1.8~~ | ~~1.6~~ | ~~3.8~~ | ~~3.6~~ | ~~6.7~~ | **~~62.3~~** | **~~62.8~~** | **~~64.5~~** | ~~26.1~~ | ~~27.5~~ | ~~23.8~~ | ~~5.9~~ | ~~4.3~~ | ~~3.4~~ |
| | ~~FYI~~ | ~~4.2~~ | ~~3.6~~ | ~~2.4~~ | ~~2.6~~ | ~~2.6~~ | ~~2.1~~ | ~~21.7~~ | ~~20.6~~ | ~~15.6~~ | **~~58.1~~** | **~~61.1~~** | **~~69.8~~** | ~~13.4~~ | ~~12.1~~ | ~~10.1~~ |
| | ~~OI~~ | ~~0.3~~ | ~~0.3~~ | ~~0.4~~ | ~~0.6~~ | ~~0.8~~ | ~~1.4~~ | ~~5.8~~ | ~~5.0~~ | ~~3.0~~ | ~~7.3~~ | ~~7.3~~ | ~~4.1~~ | **~~86.0~~** | **~~86.7~~** | **~~91.2~~** |

**Table 3: Confusion matrix of the five-class RF classifier which was trained with and applied to the DS1 winter dataset**

| | | Predicted | | | | | | | | | | | | | | |
|---|---|---|---|---|---|---|---|---|---|---|---|---|---|---|---|---|
| | | OW (open water) | | | NI (new ice) | | | YI (young ice) | | | FYI (first-year ice) | | | OI (old ice) | | |
| | case | FC1 | FC2 | FC3 | FC1 | FC2 | FC3 | FC1 | FC2 | FC3 | FC1 | FC2 | FC3 | FC1 | FC2 | FC3 |
| Actual | OW | **90.1** | **91.3** | **92.4** | 1.3 | 1.1 | 1.2 | 1.6 | 1.7 | 1.6 | 6.9 | 5.9 | 4.8 | 0.0 | 0.0 | 0.0 |
| | NI | 30.0 | 28.0 | 26.1 | **21.9** | **23.8** | **45.0** | 27.1 | 26.7 | 13.3 | 16.7 | 17.7 | 11.8 | 4.2 | 3.9 | 3.8 |
| | YI | 3.7 | 3.7 | 3.9 | 5.1 | 4.8 | 5.2 | **58.8** | **60.1** | **62.6** | 24.3 | 24.0 | 21.1 | 8.1 | 7.4 | 7.2 |
| | FYI | 5.0 | 4.7 | 3.9 | 1.7 | 1.5 | 1.7 | 18.7 | 19.0 | 19.4 | **64.4** | **65.3** | **65.9** | 10.1 | 9.6 | 9.1 |
| | OI | 0.1 | 0.1 | 0.2 | 0.3 | 0.3 | 0.6 | 3.1 | 2.9 | 3.0 | 6.4 | 6.1 | 5.6 | **90.1** | **90.6** | **90.6** |

~~**Table 3: Confusion matrix of the five-class RF classifier which was trained with 2018 dataset and applied to the 2019 dataset**~~

| | | ~~Predicted~~ | | | | | | | | | | | | | | |
|---|---|---|---|---|---|---|---|---|---|---|---|---|---|---|---|---|
| | | ~~OW (open water)~~ | | | ~~NI (new ice)~~ | | | ~~YI (young ice)~~ | | | ~~FYI (first-year ice)~~ | | | ~~OI (old ice)~~ | | |
| | ~~case~~ | ~~FC1~~ | ~~FC2~~ | ~~FC3~~ | ~~FC1~~ | ~~FC2~~ | ~~FC3~~ | ~~FC1~~ | ~~FC2~~ | ~~FC3~~ | ~~FC1~~ | ~~FC2~~ | ~~FC3~~ | ~~FC1~~ | ~~FC2~~ | ~~FC3~~ |
| ~~Actual~~ | ~~OW~~ | ~~**90.1**~~ | ~~**90.6**~~ | ~~**85.4**~~ | ~~3.1~~ | ~~2.7~~ | ~~5.7~~ | ~~1.0~~ | ~~1.1~~ | ~~2.0~~ | ~~5.8~~ | ~~5.7~~ | ~~6.9~~ | ~~0.0~~ | ~~0.0~~ | ~~0.0~~ |
| | ~~NI~~ | ~~20.1~~ | ~~24.5~~ | ~~28.3~~ | ~~**28.0**~~ | ~~**23.0**~~ | ~~**23.9**~~ | ~~42.0~~ | ~~42.4~~ | ~~40.9~~ | ~~7.6~~ | ~~7.9~~ | ~~5.5~~ | ~~2.4~~ | ~~2.1~~ | ~~1.4~~ |
| | ~~YI~~ | ~~6.7~~ | ~~6.1~~ | ~~6.3~~ | ~~3.3~~ | ~~3.4~~ | ~~3.1~~ | ~~**44.7**~~ | ~~**44.6**~~ | ~~**51.5**~~ | ~~36.0~~ | ~~38.2~~ | ~~33.5~~ | ~~9.3~~ | ~~7.7~~ | ~~5.7~~ |
| | ~~FYI~~ | ~~5.4~~ | ~~4.4~~ | ~~4.9~~ | ~~3.6~~ | ~~3.8~~ | ~~2.7~~ | ~~25.8~~ | ~~25.3~~ | ~~27.5~~ | ~~**38.9**~~ | ~~**42.0**~~ | ~~**46.0**~~ | ~~26.3~~ | ~~24.5~~ | ~~18.9~~ |
| | ~~OI~~ | ~~0.5~~ | ~~0.5~~ | ~~0.5~~ | ~~1.3~~ | ~~1.2~~ | ~~0.7~~ | ~~2.7~~ | ~~3.0~~ | ~~7.7~~ | ~~2.8~~ | ~~3.6~~ | ~~24.9~~ | ~~**92.7**~~ | ~~**91.7**~~ | ~~**66.3**~~ |

**Table 4: Confusion matrix of the five-class RF classifier which was trained with DS1 winter dataset and applied to the DS2 winter dataset**

| | | Predicted | | | | | | | | | | | | | | |
|---|---|---|---|---|---|---|---|---|---|---|---|---|---|---|---|---|
| | | OW (open water) | | | NI (new ice) | | | YI (young ice) | | | FYI (first-year ice) | | | OI (old ice) | | |
| | case | FC1 | FC2 | FC3 | FC1 | FC2 | FC3 | FC1 | FC2 | FC3 | FC1 | FC2 | FC3 | FC1 | FC2 | FC3 |
| Actual | OW | **89.1** | **90.2** | **90.3** | 1.3 | 1.1 | 1.9 | 3.3 | 3.5 | 4.2 | 6.4 | 5.2 | 3.7 | 0.0 | 0.0 | 0.0 |
| | NI | 45.1 | 45.0 | 56.5 | **31.9** | **30.6** | **17.6** | 6.0 | 5.7 | 13.3 | 15.1 | 17.3 | 11.2 | 2.0 | 1.5 | 1.5 |
| | YI | 7.1 | 7.1 | 9.2 | 6.3 | 5.9 | 8.5 | **47.6** | **48.0** | **55.0** | 28.7 | 29.2 | 17.3 | 10.4 | 9.8 | 9.9 |
| | FYI | 5.6 | 5.0 | 5.8 | 3.8 | 3.5 | 3.2 | 32.8 | 33.0 | 35.0 | **38.4** | **39.7** | **37.3** | 19.3 | 18.8 | 18.7 |
| | OI | 0.3 | 0.3 | 0.7 | 0.5 | 0.4 | 0.7 | 1.9 | 1.8 | 1.9 | 4.6 | 4.8 | 4.5 | **92.8** | **92.8** | **92.6** |

~~**Table 4: Classification accuracies before and after applying textural denoising**~~

| ~~class~~ | ~~case~~ | | | | | | | | |
|---|---|---|---|---|---|---|---|---|---|
| | ~~FC1~~ | | | ~~FC2~~ | | | ~~FC3~~ | | |
| | ~~Thermal denoising only~~ | ~~Textural denoising applied~~ | ~~difference~~ | ~~Thermal denoising only~~ | ~~Textural denoising applied~~ | ~~difference~~ | ~~Thermal denoising only~~ | ~~Textural denoising applied~~ | ~~difference~~ |
| ~~OW~~ | ~~88.4~~ | ~~90.1~~ | ~~+1.7~~ | ~~88.9~~ | ~~90.6~~ | ~~+1.7~~ | ~~88.0~~ | ~~85.4~~ | ~~-2.6~~ |
| ~~NI~~ | ~~30.2~~ | ~~28.0~~ | ~~-2.8~~ | ~~27.7~~ | ~~23.0~~ | ~~-4.7~~ | ~~31.8~~ | ~~23.9~~ | ~~-7.9~~ |
| ~~YI~~ | ~~34.9~~ | ~~44.7~~ | ~~+9.8~~ | ~~36.2~~ | ~~44.6~~ | ~~+8.2~~ | ~~43.4~~ | ~~51.5~~ | ~~+8.1~~ |
| ~~FYI~~ | ~~29.3~~ | ~~38.9~~ | ~~+9.6~~ | ~~30.4~~ | ~~42.0~~ | ~~+11.6~~ | ~~38.0~~ | ~~47.0~~ | ~~+9.0~~ |
| ~~OI~~ | ~~91.5~~ | ~~92.7~~ | ~~+1.2~~ | ~~90.3~~ | ~~91.7~~ | ~~+1.4~~ | ~~75.2~~ | ~~66.3~~ | ~~-8.9~~ |
| ~~kappa~~ | ~~0.62~~ | ~~0.67~~ | ~~+0.05~~ | ~~0.62~~ | ~~0.67~~ | ~~+0.05~~ | ~~0.54~~ | ~~0.49~~ | ~~-0.05~~ |

**Table 5: Classification accuracies before and after applying textural denoising**

| class | case | | | | | | | | |
|---|---|---|---|---|---|---|---|---|---|
| | FC1 | | | FC2 | | | FC3 | | |
| | Thermal denoising only | Textural denoising applied | difference | Thermal denoising only | Textural denoising applied | difference | Thermal denoising only | Textural denoising applied | difference |
| Open water | 88.0 | 89.1 | +1.1 | 88.7 | 90.2 | +1.5 | 89.4 | 90.3 | +1.9 |
| New ice | 32.2 | 31.9 | -0.3 | 32.2 | 30.6 | -1.6 | 20.0 | 17.6 | -2.4 |
| Young ice | 45.2 | 47.6 | +2.4 | 44.7 | 48.0 | +3.3 | 48.8 | 55.0 | +6.2 |
| First-year ice | 38.6 | 38.4 | -0.2 | 39.4 | 39.7 | +0.3 | 36.4 | 37.3 | +0.9 |
| Old ice | 88.9 | 92.8 | +3.9 | 88.3 | 92.8 | +4.5 | 88.6 | 92.6 | +4.0 |
| kappa | 0.59 | 0.67 | +0.08 | 0.59 | 0.67 | +0.08 | 0.59 | 0.67 | +0.08 |

**Table 6: Confusion matrix of the three-class RF classifier which was trained with and applied to the DS1 summer dataset**

| | | Predicted | | | | | | | | |
|---|---|---|---|---|---|---|---|---|---|---|
| | | OW (open water) | | | mFYI (mixed first-year ice) | | | OI (old ice) | | |
| | Case | FC1 | FC2 | FC3 | FC1 | FC2 | FC3 | FC1 | FC2 | FC3 |
| Actual | OW | **98.1** | **97.9** | **98.7** | 0.7 | 0.7 | 0.6 | 1.2 | 1.4 | 0.6 |
| | mFYI | 4.1 | 3.9 | 2.4 | **14.9** | **15.5** | **41.8** | 81.1 | 80.6 | 55.8 |
| | OI | 1.5 | 1.4 | 1.0 | 5.5 | 5.7 | 4.9 | **93.0** | **92.9** | **94.1** |

**Table 7: Confusion matrix of the three-class RF classifier which was trained with DS1 summer dataset and applied to the DS2 summer dataset**

| | | Predicted | | | | | | | | |
|---|---|---|---|---|---|---|---|---|---|---|
| | | OW (open water) | | | mFYI (mixed first-year ice) | | | OI (old ice) | | |
| | Case | FC1 | FC2 | FC3 | FC1 | FC2 | FC3 | FC1 | FC2 | FC3 |
| Actual | OW | **99.5** | **99.4** | **96.2** | 0.2 | 0.2 | 3.2 | 0.3 | 0.4 | 0.6 |
| | mFYI | 5.4 | 5.1 | 3.0 | **12.0** | **11.2** | **25.8** | 82.5 | 83.7 | 71.2 |
| | OI | 2.9 | 2.7 | 2.2 | 5.8 | 5.8 | 13.4 | **91.2** | **91.4** | **84.4** |

~~**Table 5: Confusion matrix of the three-class RF classifier which were trained and applied to the 2018 dataset**~~

| | | ~~Predicted~~ | | | | | | | | |
|---|---|---|---|---|---|---|---|---|---|---|
| | | ~~OW (open water)~~ | | | ~~mFYI (mixed FYI)~~ | | | ~~OI (old ice)~~ | | |
| | ~~Case~~ | ~~FC1~~ | ~~FC2~~ | ~~FC3~~ | ~~FC1~~ | ~~FC2~~ | ~~FC3~~ | ~~FC1~~ | ~~FC2~~ | ~~FC3~~ |
| ~~Actual~~ | ~~OW~~ | ~~**96.7**~~ | ~~**97.3**~~ | ~~**99.1**~~ | ~~3.3~~ | ~~2.6~~ | ~~0.9~~ | ~~0.0~~ | ~~0.0~~ | ~~0.0~~ |
| | ~~mFYI~~ | ~~5.2~~ | ~~4.7~~ | ~~2.5~~ | ~~**85.8**~~ | ~~**87.6**~~ | ~~**92.3**~~ | ~~9.0~~ | ~~7.7~~ | ~~5.2~~ |
| | ~~OI~~ | ~~0.4~~ | ~~0.4~~ | ~~0.2~~ | ~~13.2~~ | ~~12.4~~ | ~~6.0~~ | ~~**86.4**~~ | ~~**87.2**~~ | ~~**93.8**~~ |

**Table 8: Confusion matrix of the three-class RF classifier which were trained and applied to the DS1 winter dataset**

| | | Predicted | | | | | | | | |
|---|---|---|---|---|---|---|---|---|---|---|
| | | OW (open water) | | | mFYI (mixed first-year ice) | | | OI (old ice) | | |
| | Case | FC1 | FC2 | FC3 | FC1 | FC2 | FC3 | FC1 | FC2 | FC3 |
| Actual | OW | **92.2** | **92.5** | **93.6** | 7.8 | 7.4 | 6.3 | 0.0 | 0.0 | 0.0 |
| | mFYI | 6.4 | 5.5 | 5.5 | **83.8** | **85.3** | **85.5** | 9.8 | 9.2 | 9.0 |
| | OI | 0.2 | 0.2 | 0.2 | 8.9 | 8.5 | 8.7 | **90.9** | **91.3** | **91.1** |

~~**Table 6: Confusion matrix of the three-class RF classifier which was trained with the 2018 dataset and applied to the 2019 dataset**~~

| | | ~~Predicted~~ | | | | | | | | |
|---|---|---|---|---|---|---|---|---|---|---|
| | | ~~OW (open water)~~ | | | ~~mFYI (mixed FYI)~~ | | | ~~OI (old ice)~~ | | |
| | ~~Case~~ | ~~FC1~~ | ~~FC2~~ | ~~FC3~~ | ~~FC1~~ | ~~FC2~~ | ~~FC3~~ | ~~FC1~~ | ~~FC2~~ | ~~FC3~~ |
| ~~Actual~~ | ~~OW~~ | ~~**93.6**~~ | ~~**93.6**~~ | ~~**86.3**~~ | ~~6.4~~ | ~~6.4~~ | ~~13.6~~ | ~~0.0~~ | ~~0.0~~ | ~~0.0~~ |
| | ~~mFYI~~ | ~~8.8~~ | ~~7.5~~ | ~~7.1~~ | ~~**72.4**~~ | ~~**75.3**~~ | ~~**81.6**~~ | ~~18.8~~ | ~~17.2~~ | ~~11.3~~ |
| | ~~OI~~ | ~~0.6~~ | ~~0.6~~ | ~~0.4~~ | ~~6.7~~ | ~~8.1~~ | ~~39.8~~ | ~~**92.7**~~ | ~~**91.4**~~ | ~~**59.7**~~ |

**Table 9: Confusion matrix of the three-class RF classifier which was trained with the DS1 winter dataset and applied to the DS2 winter dataset**

| | | Predicted | | | | | | | | |
|---|---|---|---|---|---|---|---|---|---|---|
| | | OW (open water) | | | mFYI (mixed first-year ice) | | | OI (old ice) | | |
| | Case | FC1 | FC2 | FC3 | FC1 | FC2 | FC3 | FC1 | FC2 | FC3 |
| Actual | OW | **91.4** | **91.7** | **91.7** | 8.6 | 8.3 | 8.3 | 0.0 | 0.0 | 0.0 |
| | mFYI | 9.4 | 8.3 | 9.9 | **75.0** | **76.5** | **74.6** | 15.6 | 15.2 | 15.5 |
| | OI | 0.3 | 0.3 | 0.3 | 6.3 | 6.5 | 6.6 | **93.3** | **93.2** | **93.1** |

**Table 10: Confusion matrix of the three-class RF classifier which was trained with DS1 winter dataset and applied to the DS2 winter dataset with reference to OSI SAF sea ice type product (OSI-403-c)**

| | | Predicted (classifier was trained with NIC ice chart) | | | | | | | | |
|---|---|---|---|---|---|---|---|---|---|---|
| | | Open water | | | Mixed first-year ice | | | Old ice | | |
| | Case | FC1 | FC2 | FC3 | FC1 | FC2 | FC3 | FC1 | FC2 | FC3 |
| Reference (OSI SAF) | Open water | **85.9** | **86.1** | **86.2** | 12.6 | 12.4 | 12.1 | 15.7 | 15.3 | 16.2 |
| | First-year ice | 1.9 | 1.6 | 2.0 | **26.0** | **26.8** | **26.9** | 72.1 | 71.6 | 71.2 |
| | Multi-year ice | 0.1 | 0.1 | 0.1 | 1.5 | 1.4 | 1.4 | **98.4** | **98.5** | **98.5** |